The Low-redshift Lyman Continuum Survey. II. New Insights into LyC Diagnostics

Sophia R. Flury, Anne E. Jaskot, Harry C. Ferguson, Gábor Worseck, Kirill Makan, John Chisholm, Alberto Saldana-Lopez, Daniel Schaerer, Stephan R. Mccandliss, Xinfeng Xu, et al.

The Astrophysical Journal, 930:126 (21pp), 2022 May 10 https://doi.org/10.3847/1538-4357/ac61e4

The Low-redshift Lyman Continuum Survey. II. New Insights into LyC Diagnostics

Sophia R. Flury[1], Anne E. Jaskot[2], Harry C. Ferguson[3], Gábor Worseck[4], Kirill Makan[4], John Chisholm[5], Alberto Saldana-Lopez[6], Daniel Schaerer[6], Stephan R. McCandliss[7], Xinfeng Xu[8], Bingjie Wang[8], M. S. Oey[9], N. M. Ford[2], Timothy Heckman[8], Zhiyuan Ji[1], Mauro Giavalisco[1], Ricardo Amorín[10,11], Hakim Atek[12], Jeremy Blaizot[13], Sanchayeeta Borthakur[14], Cody Carr[15], Marco Castellano[16], Stephane De Barros[6], Mark Dickinson[17], Steven L. Finkelstein[5], Brian Fleming[18], Fabio Fontanot[19], Thibault Garel[6], Andrea Grazian[20], Matthew Hayes[21], Alaina Henry[3], Valentin Mauerhofer[6,22], Genoveva Micheva[23], Goran Ostlin[21], Casey Papovich[24], Laura Pentericci[16], Swara Ravindranath[3], Joakim Rosdahl[13], Michael Rutkowski[25], Paola Santini[16], Claudia Scarlata[15], Harry Teplitz[26], Trinh Thuan[27], Maxime Trebitsch[28], Eros Vanzella[29], and Anne Verhamme[6,22]

[1] Department of Astronomy, University of Massachusetts Amherst, Amherst, MA 01002, USA; sflury@umass.edu
[2] Department of Astronomy, Williams College, Williamstown, MA 01267, USA
[3] Space Telescope Science Institute, 3700 San Martin Drive, Baltimore, MD 21218, USA
[4] Institut für Physik und Astronomie, Universität Potsdam, Karl-Liebknecht-Str. 24/25, D-14476 Potsdam, Germany
[5] Department of Astronomy, University of Texas at Austin, Austin, TX 78712, USA
[6] Observatoire de Genève, Université de Genève, 51 Ch. des Mailletes, 1290 Versoix, Switzerland
[7] Center for Astrophysical Sciences Department of Physics and Astronomy, Johns Hopkins University, 3400 North Charles Street, Baltimore, MD 21218, USA
[8] Department of Physics and Astronomy, Johns Hopkins University, Baltimore, MD 21218, USA
[9] Department of Astronomy, University of Michigan, Ann Arbor, MI 48109, USA
[10] Instituto de Investigación Multidisciplinar en Ciencia y Tecnología, Universidad de La Serena, Raúl Bitrán 1305, La Serena, Chile
[11] Departamento de Astronomía, Universidad de La Serena, Av. Juan Cisternas 1200 Norte, La Serena, Chile
[12] Institut d'astrophysique de Paris, CNRS UMR7095, Sorbonne Université, 98bis Boulevard Arago, F-75014 Paris, France
[13] Univ Lyon, Univ Lyon1, Ens de Lyon, CNRS, Centre de Recherche Astrophysique de Lyon UMR5574, F-69230, Saint-Genis-Laval, France
[14] School of Earth & Space Exploration, Arizona State University, Tempe, AZ 85287, USA
[15] Minnesota Institute for Astrophysics, School of Physics and Astronomy, University of Minnesota, 316 Church St. SE, Minneapolis, MN 55455, USA
[16] INAF, Osservatorio Astronomico di Roma, via Frascati 33, I-00078 Monteporzio Catone, Italy
[17] National Optical-Infrared Astronomy Research Laboratory, Tucson, AZ 85721, USA
[18] Laboratory for Atmospheric and Space Physics, Boulder, CO, USA
[19] INAF, Osservatorio Astronomico di Trieste, Via G.B. Tiepolo, 11, I-34143 Trieste, Italy
[20] INAF, Osservatorio Astronomico di Padova, Vicolo dell Osservatorio 5, I-35122, Padova, Italy
[21] The Oskar Klein Centre, Department of Astronomy, Stockholm University, AlbaNova, SE-10691 Stockholm, Sweden
[22] Univ. Lyon, Univ. Lyon 1, ENS de Lyon, CNRS, Centre de Recherche Astrophysique de Lyon UMR5574, F-69230 Saint-Genis-Laval, France
[23] Leibniz-Institute for Astrophysics Potsdam, An der Sternwarte 16, D-14482 Potsdam, Germany
[24] George P. and Cynthia Woods Mitchell Institute for Fundamental Physics and Astronomy, Department of Physics and Astronomy, Texas A&M University, College Station, TX 77843, USA
[25] Department of Physics and Astronomy, Minnesota State University, Mankato, MN 56001, USA
[26] Infrared Processing and Analysis Center, California Institute of Technology, Pasadena, CA 91125, USA
[27] Astronomy Department, University of Virginia, Charlottesville, VA 22904, USA
[28] Astronomy, Kapteyn Astronomical Institute, Landleven 12, 9747 AD Groningen, The Netherlands
[29] INAF, Osservatorio Astronomico di Bologna, via Gobetti 93/3 I-40129 Bologna, Italy
Received 2021 August 5; revised 2022 March 16; accepted 2022 March 26; published 2022 May 11

Abstract

The Lyman continuum (LyC) cannot be observed at the epoch of reionization ($z \gtrsim 6$) owing to intergalactic H I absorption. To identify LyC emitters (LCEs) and infer the fraction of escaping LyC, astronomers have developed various indirect diagnostics of LyC escape. Using measurements of the LyC from the Low-redshift Lyman Continuum Survey (LzLCS), we present the first statistical test of these diagnostics. While optical depth indicators based on Lyα, such as peak velocity separation and equivalent width, perform well, we also find that other diagnostics, such as the [O III]/[O II] flux ratio and star formation rate surface density, predict whether a galaxy is an LCE. The relationship between these galaxy properties and the fraction of escaping LyC flux suggests that LyC escape depends strongly on H I column density, ionization parameter, and stellar feedback. We find that LCEs occupy a range of stellar masses, metallicities, star formation histories, and ionization parameters, which may indicate episodic and/or different physical causes of LyC escape.

Unified Astronomy Thesaurus concepts: Reionization (1383); Galactic and extragalactic astronomy (563); Hubble Space Telescope (761); Ultraviolet astronomy (1736); Emission line galaxies (459)

1. Introduction

While the reionization of the universe likely completed by a redshift of $z \sim 6$ (e.g., Becker et al. 2001; Paoletti et al. 2020; Pahl et al. 2020; Yang et al. 2020), substantial contention persists concerning which galaxies are responsible. Intense, concentrated star formation seems to be a necessary characteristic of reionizing galaxies because of the associated stellar feedback (e.g., Heckman et al. 2001; Clarke & Oey 2002; Heckman et al. 2011; Sharma et al. 2017; Naidu et al. 2020). Many predictions suggest that dwarf galaxies are the primary Lyman continuum (LyC) photon donors because the weak

gravitational potentials of low-mass galaxies exacerbate the clearing effects of feedback (e.g., Razoumov & Sommer-Larsen 2010; Wise et al. 2014; Paardekooper et al. 2015; Izotov et al. 2021). Others indicate that more massive galaxies dominate reionization because stronger gravitational potentials better facilitate efficient star formation, resulting in a higher LyC photon budget (e.g., Wyithe & Loeb 2013). An increase in dust extinction with galaxy mass could reduce LyC escape at the highest masses, causing galaxies with masses in between these two regimes to dominate reionization (e.g., Ma et al. 2020).

Central to this debate is the fraction of LyC photons that escape from a galaxy to reionize the intergalactic medium (IGM). This "escape fraction" $f_{\rm esc}^{\rm LyC}$ relates the cosmic star formation rate (SFR) density and LyC production efficiency to the cosmic ionization rate. Based on results from stacked spectra at $z\sim3$ (e.g., Steidel et al. 2018) and from cosmological simulations (e.g., Finkelstein et al. 2012), galaxies that exhibit $f_{\rm esc}^{\rm LyC}\gtrsim0.05$ are the most relevant to reionization. Due to the increase in intergalactic LyC absorption with redshift, direct measurement of the LyC, let alone $f_{\rm esc}^{\rm LyC}$, is statistically unlikely beyond $z\sim4$ (e.g., Vanzella et al. 2012; Worseck et al. 2014) to ascertain which galaxies are responsible for reionizing the universe.

Therefore, we must study lower-redshift LyC-leaking galaxies to develop indirect diagnostics for $f_{\rm esc}^{\rm LyC}$. These diagnostics may also provide insight into the physical mechanism(s) and environmental conditions that contribute to leaking of LyC photons. In the following, we will explore some of the most promising diagnostics for $f_{\rm esc}^{\rm LyC}$, including the equivalent widths (EWs) of nebular emission lines, emission-line flux ratios, the profile of the Lyα emission line, the SFR surface density ($\Sigma_{\rm SFR}$), and the UV continuum slope (β) and magnitude (M_{1500}).

Of these properties, nebular emission-line EWs are one of the easiest to measure. Because hydrogen Balmer lines originate from recombination across the entire extent of H II regions, measuring a smaller EW in these lines may indicate lower optical depth: if gas does not extend out to the Strömgren radius, not all LyC photons will photoionize H I, and thus the nebula will emit fewer Balmer photons (e.g., Bergvall et al. 2013). To date, few tests of this diagnostic have been conducted. Moreover, many local LyC emitters (LCEs) exhibiting high Balmer emission line EWs have been found (Izotov et al. 2016b, 2018a, 2018b). In any case, Balmer-line EWs are sensitive not only to nebula size but also to starburst age and star formation history (Zackrisson et al. 2017; Binggeli et al. 2018; Alavi et al. 2020). Plagued by such degeneracies, the EW diagnostic may be best when paired with another indicator.

Similarly motivated by optical depth, the emission-line flux ratio $O_{32}=$ [O III] $\lambda5007/$[O II] $\lambda\lambda3726, 3729$ probes the relative sizes of the O^{+2} and O^{+} ionized zones. When the nebula is optically thin to LyC, the O^{+} zone will be smaller relative to the O^{+2} zone (Jaskot & Oey 2013; Nakajima & Ouchi 2014). Albeit straightforward, O_{32} also depends strongly on ionization parameter to the extent that O_{32} is commonly used to measure it (e.g., Kobulnicky & Kewley 2004; Stasińska et al. 2015; Strom et al. 2018). It is unclear whether this dependence will obfuscate $f_{\rm esc}^{\rm LyC}$ diagnostics. For instance, $f_{\rm esc}^{\rm LyC}$ itself may depend on ionization parameter if the incident stellar radiation field is responsible for a density-bounded scenario wherein gas does not persist out to the Strömgren radius. O_{32} also does not probe the outer extent of the nebula, the region that is most sensitive to optical depth. Observationally, there is substantial scatter in the $f_{\rm esc}^{\rm LyC}-O_{32}$ relation (e.g., Izotov et al. 2018b), making this diagnostic tenuous.

Complementing the O_{32} diagnostic, the [O I] $\lambda6300$ emission line traces neutral gas at the outer extent of a nebula because O^0 has an ionization potential similar to that of hydrogen (13.62 eV) and is coupled to hydrogen recombination by charge exchange reactions (Osterbrock & Ferland 2006). Comparing the [O I] $\lambda6300$ flux to the flux of another emission line can thus indicate the prevalence of neutral gas at the nebula boundary. Stasińska et al. (2015) consider the $O_{31}=$ [O III] $\lambda5007/$[O I] $\lambda6300$ flux ratio as a diagnostic for LyC escape. They argue that, while sensitive to physical conditions and other ionization sources, O_{31} could indicate a density-bounded nebula, as it traces the size of the O^0 zone relative to the O^{+2} zone. Similarly, the [O I]/Hβ ratio could indicate a deficiency in neutral gas relative to hydrogen recombining from H II to H I across the nebula, comparable to the effect described by Wang et al. (2019) for [S II]/Hα. The [O I] line is not without complications, though. In models where LyC optical depth and ionization parameter are not constant across the nebula (the so-called "picket fence" scenario; see Heckman et al. 2001), Ramambason et al. (2020) predict that O_{31} and [O I]/Hβ depend on conditions such as starburst age, ionization parameter, and LyC escape conditions. Shocks can also produce [O I] emission, further complicating the [O I] line as a diagnostic. Even so, these [O I] flux ratios have promise as indicators of $f_{\rm esc}^{\rm LyC}$. Jaskot et al. (2019) found that both flux ratios correlate with the Lyα profile peak velocity separation, itself an indicator of $f_{\rm esc}^{\rm LyC}$(e.g., Izotov et al. 2018b).

The Lyα recombination emission line is sensitive to the neutral H I opacity of a galaxy (e.g., Behrens et al. 2014; Verhamme et al. 2015). First, the shape of the Lyα profile depends on the amount of both absorption and reemission of Lyα photons by H I in the host galaxy (essentially a "scattering" effect; e.g., Verhamme et al. 2017; Gazagnes et al. 2020). Second, the line-of-sight H I column density affects the fraction of Lyα photons that escape (e.g., Henry et al. 2015; Yang et al. 2017a; Izotov et al. 2018b). The discovery of triple-peaked Lyα profiles associated with LCEs (e.g., Rivera-Thorsen et al. 2019; Izotov et al. 2018b; Vanzella et al. 2020) suggests low optical depth cavities in the interstellar medium (ISM) facilitating both Lyα and LyC photon escape (Byrohl & Gronke 2020). While these results are promising, the Lyα line can be sensitive to IGM extinction, metallicity, and stellar populations in the host galaxy (e.g., Henry et al. 2015; Yang et al. 2017a). Moreover, the increasing IGM neutral covering can significantly extinguish Lyα at high redshifts (e.g., Pentericci et al. 2011; Schenker et al. 2014), particularly the blue peak in the emission-line profile (e.g., Laursen et al. 2011; Yang et al. 2017b; Hayes et al. 2021). Focusing on Lyα emitters may additionally introduce a sampling bias since a nonnegligible fraction of high-redshift Lyman break galaxies (LBGs) and some LCEs exhibit little to no Lyα (e.g., Vanzella et al. 2009; Ji et al. 2020). Nevertheless, at reionization, Lyα falls in an ideal ground-based observing window (Bagley et al. 2017; Yajima et al. 2018), making Lyα more feasible a diagnostic of $f_{\rm esc}^{\rm LyC}$ than rest-frame optical lines.

SFR surface density, on the other hand, may serve simultaneously as a probe of the physical mechanism of LyC leakage and a as proxy for $f_{\rm esc}^{\rm LyC}$. Feedback from star formation can blow bubbles/chimneys in the host galaxy's ISM (e.g., Heckman et al. 2001; Clarke & Oey 2002; Sharma et al. 2016; Naidu et al. 2020; Gazagnes et al. 2020), suggesting that high $\Sigma_{\rm SFR}$ will correspond to high $f_{\rm esc}^{\rm LyC}$. Previously detected LCEs also appear to be compact (e.g., Izotov et al. 2018b; Marchi et al. 2018). Compactness indicates concentrated star formation and may correlate with LyC emission (e.g., Marchi et al. 2018), although it is yet unclear whether this is a defining characteristic of all LCEs. High $\Sigma_{\rm SFR}$ appears to correlate with weaker low-ionization metal absorption lines (e.g., Alexandroff et al. 2015), which suggests a connection with low optical depth.

All the diagnostics outlined above are plausible but remain, as of yet, insufficiently explored owing to small sample sizes. Future observations with the James Webb Space Telescope (JWST) and other observatories require reliable indirect diagnostics to infer $f_{\rm esc}^{\rm LyC}$ at reionization. The recent Low-redshift Lyman Continuum Survey (LzLCS; Flury et al. 2022, hereafter Paper I) presents an unprecedented opportunity to investigate the properties of nearby ($z\sim0.3$) LCEs to test each diagnostic. In this paper, we summarize the survey in Section 2 but refer the reader to Paper I for details. We provide assessments of the success of indirect diagnostics for selecting LCEs and inferring $f_{\rm esc}^{\rm LyC}$ (Section 3). In Section 4, we compare different parameters and consider the implications both for diagnostics and for populations of LCEs. Finally, we discuss our results in the contexts of different LyC escape scenarios, cosmological simulations, and high-redshift surveys in Section 5. As in Paper I, we assume $H_0=70\,{\rm km\,s^{-1}\,Mpc^{-1}}$, $\Omega_m=0.3$, and $\Omega_\Lambda=0.7$.

2. The LzLCS Sample

In Paper I, we outline the LzLCS sample selection, data processing, LyC measurements, and ancillary measurements. Here we summarize the LzLCS but refer the reader to Paper I for details. The LzLCS consists of Hubble Space Telescope (HST)/COS G140L observations of 66 new LCE candidates in the nearby ($z\sim0.3$–0.4) universe. The significance of the LzLCS over previous surveys is not just its size but also its scope: the LzLCS spans a much broader range in, among other properties, O_{32}, UV β, $\Sigma_{\rm SFR}$, stellar mass, metallicity, and burst age than prior studies.

From the COS spectra, we measure the LyC and Lyα flux, the Lyα EW, and the spectral slope of the attenuated starlight continuum. To assess the detection of the LyC, we define the probability $P(>N|B)$ given by the Poisson survival function that the observed signal arises by chance from background fluctuations (see Worseck et al. 2016; Makan et al. 2021). In summary, we detect LyC emission from 35 galaxies at >97.725% confidence ($P(>N|B)<0.02275$, $>2\sigma$ significance), with 13/35 of these galaxies having fairly detected LyC flux ($P(>N|B)<0.00135$, 3σ–5σ significance) and 12/35 of these galaxies having well-detected LyC flux ($P(>N|B)<2.867\times10^{-7}$, $>5\sigma$ significance). Following Chisholm et al. (2019), we also perform spectral energy distribution (SED) fitting using instantaneous burst model spectra from STARBURST99 (Leitherer et al. 2010) to infer the intrinsic and observed UV magnitudes at 1500 Å, starlight attenuation, starburst age, and intrinsic LyC flux (see Saldana-Lopez et al. 2022, for details). From the COS acquisition images, we determine the UV half-light radius from the background-subtracted empirical cumulative light distribution, which is consistent with results from Sérsic profile fits.

Optical spectra from the Sloan Digital Sky Survey (SDSS) provide additional information. We measure nebular emission-line fluxes and EWs from these spectra. To correct the fluxes for reddening, we infer nebular extinction from Balmer lines assuming Case B recombination with Storey & Hummer (1995) atomic data and the Cardelli et al. (1989) reddening law. From the extinction-corrected fluxes, we obtain diagnostic flux ratios like O_{32}. Since [O III] $\lambda4363$ is detected in the majority of the galaxies in our sample, we determine gas-phase metallicities by the direct method, inferring the auroral line flux by the flux–flux relation (Pilyugin et al. 2006) when not available.

Combining the SDSS and COS measurements with GALEX observations, we infer additional properties of the sample. We obtain stellar masses by fitting aperture-matched photometry from SDSS and GALEX using PROSPECTOR (Leja et al. 2017; Johnson et al. 2019). From the Balmer-line SFR (Kennicutt & Evans 2012), UV half-light radius, and stellar mass, we calculate the SFR surface density and specific SFR (sSFR). We subsequently correct the Balmer-line SFR quantities for the escape of ionizing photons. From the Hβ and Lyα fluxes, we also determine the fraction of Lyα photons $f_{\rm esc}^{\rm Ly\alpha}$ that have escaped the host galaxy.

As discussed in Section 1, the key objective of establishing LyC escape diagnostics is to determine which properties most strongly correlate with the LyC escape fraction $f_{\rm esc}^{\rm LyC}$. We measure $f_{\rm esc}^{\rm LyC}$ by three different methods: (i) the empirical $F_{\lambda\rm LyC}/F_{\lambda1100}$ ratio, (ii) using Hβ to infer the intrinsic LyC from STARBURST99 continuous starburst model spectra ($f_{\rm esc}^{\rm LyC}$(Hβ)), and (iii) using SED fits to the COS far-UV (FUV) spectra to infer the intrinsic LyC ($f_{\rm esc}^{\rm LyC}$(UV)). We summarize these metrics below.

1. The $F_{\lambda\rm LyC}/F_{\lambda1100}$ ratio is simply a ratio of flux density measurements and is therefore free of any assumptions. However, $F_{\lambda\rm LyC}/F_{\lambda1100}$ is sensitive to a number of factors in addition to the LyC escape fraction, including dust attenuation, SFR, metallicity, and burst age, complicating the interpretation of this quantity as a metric of $f_{\rm esc}^{\rm LyC}$.
2. The Hβ approach introduced by Izotov et al. (2016b) uses the Hβ flux, a measure of the total number of absorbed ionizing photons, the Hβ EW, a proxy for burst age, and the gas-phase metallicity to determine which STARBURST99 model to use to predict the intrinsic LyC flux density corresponding to the measured LyC. The observed LyC flux density relative to the intrinsic LyC flux density then gives the $f_{\rm esc}^{\rm LyC}$. This method can be sensitive to the assumed star formation history, particularly for older burst ages or for galaxies with high stellar mass. In Paper I, we find that a continuous star formation scenario provides the best agreement with the other two $f_{\rm esc}^{\rm LyC}$ metrics.
3. The UV approach relies on fitting the COS UV spectra over the rest-frame wavelength range of 925–1345 Å. These SED fits consist of a uniform Reddy et al. (2016) attenuation law applied to a weighted linear combination

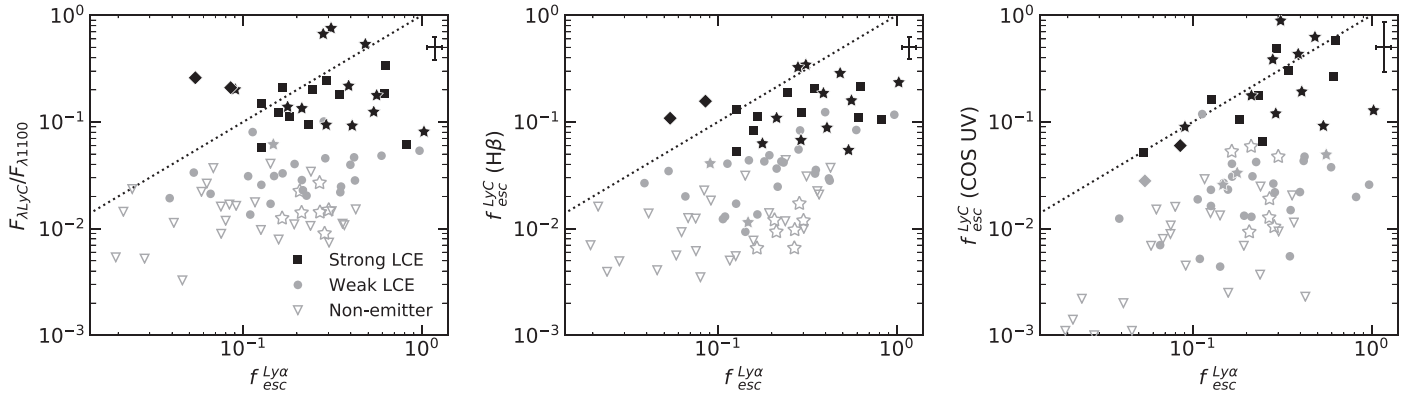

Figure 1. Comparison of $F_{\lambda LyC}/F_{\lambda 1100}$ (left), f_{esc}^{LyC} from Hβ (middle), and f_{esc}^{LyC} from fitting the COS UV spectrum (right) with $f_{esc}^{Ly\alpha}$ for strong LCEs (>5σ LyC detection and $f_{esc}^{LyC} > 0.05$; filled black), weak LCEs (>2σ LyC detection but not strong; filled gray), and nonemitters (<2σ LyC detection; open gray). For nonemitters, f_{esc}^{LyC} is shown for the 1σ upper limit on the LyC flux. LzLCS results are shown as squares (strong LCEs), circles (weak LCEs), and triangles (nondetections), while the Izotov et al. (2016a, 2016b, 2018a, 2018b, 2021) galaxies are shown as stars and the Wang et al. (2019) galaxies are shown as diamonds. Characteristic 1σ uncertainties are shown in the upper right corner. The dotted line indicates 1:1 equivalence.

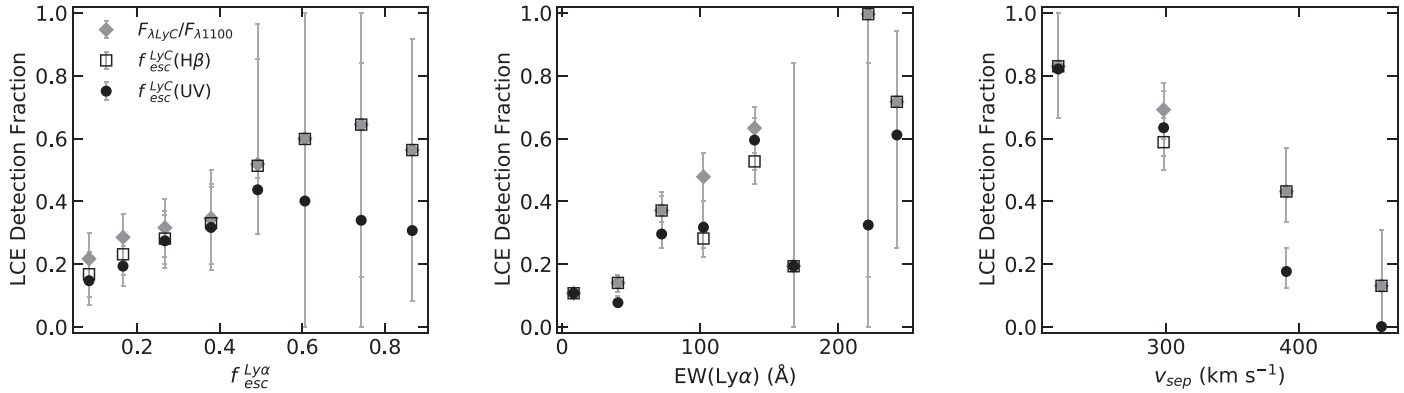

Figure 2. Fraction of galaxies in a given bin of $f_{esc}^{Ly\alpha}$ (left), EW(Lyα) (middle), or v_{sep} (right) that are strong LCEs according to $F_{\lambda LyC}/F_{\lambda 1100}$ (gray diamonds), f_{esc}^{LyC}(Hβ) (open squares), and f_{esc}^{LyC}(UV) (filled black circles) for the combined LzLCS and published samples.

of single-burst STARBURST99 spectra and accompanying nebular continua (see Chisholm et al. 2019; Saldana-Lopez et al. 2022). The best-fit SED allows us to predict the intrinsic LyC flux density, which we then use to obtain the f_{esc}^{LyC}. While the UV fits are still affected by assumptions about the star formation history and dust attenuation, the COS UV f_{esc}^{LyC} is less sensitive to systematics than the Hβ f_{esc}^{LyC}, making this metric the most reliable of the three.

We discuss the systematics and caveats of each f_{esc}^{LyC} measurement in detail in Paper I. Since each metric has its caveats, we choose to consider all three in our assessment of f_{esc}^{LyC} diagnostics below.

In addition to the 66 LzLCS galaxies, we include 23 LCE candidates that have been observed by HST/COS and previously published in other studies (Izotov et al. 2016a, 2016b, 2018a, 2018b, 2021; Wang et al. 2019). To obtain LyC fluxes and f_{esc}^{LyC} values in a consistent manner, we reprocess their HST/COS observations. Our significance estimates are comparable to the published values. However, our more stringent $P(>N|B) < 0.02275$ detection criterion includes two fewer LCEs than previous assessments, yielding a total of 15 LyC detections out of 23 published observations. For consistency, we also remeasure and infer the diagnostic properties from SDSS and COS observations in the same manner as the LzLCS galaxies. A detailed comparison of these published LCE candidates with the LzLCS is presented in Paper I.

3. Indirect f_{esc}^{LyC} Diagnostics

The LzLCS aims to test various f_{esc}^{LyC} diagnostics proposed in the literature as discussed in Section 1. To that end, we compare our measured f_{esc}^{LyC} against each parameter in Figures 1–17. As discussed in Section 2, we consider three different metrics of f_{esc}^{LyC} since each is susceptible to various systematic uncertainties. Another reason to use different f_{esc}^{LyC} indicators stems from the fact that one of the f_{esc}^{LyC} measurements is sometimes obtained from the same data as the proposed indirect diagnostics. Additional f_{esc}^{LyC} metrics allow us to assess whether an apparent correlation is real or simply introduced by using the same data in the abscissa and ordinate variables.

To quantify possible correlations, we compute the Kendall τ rank correlation coefficient following the Akritas & Siebert (1996) prescription for censored data to account for upper limits on f_{esc}^{LyC} when $P(>N|B) > 0.02275$ and any left- or right-censored indirect indicators of f_{esc}^{LyC}. For nonemitters, we use f_{esc}^{LyC} derived from the 1σ upper limit on the LyC flux for all three f_{esc}^{LyC} indicators. If we impose a 3σ detection requirement

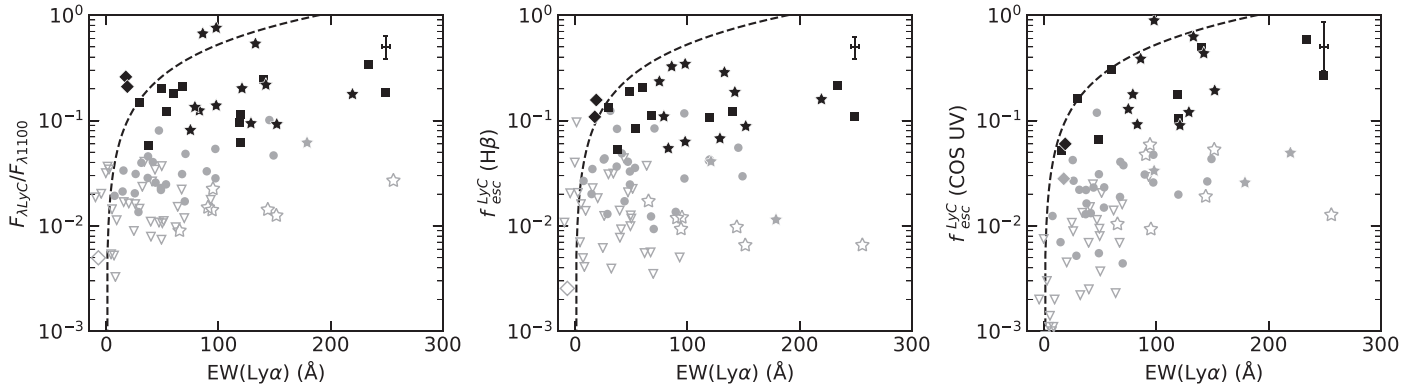

Figure 3. Same as Figure 1, but for Lyα EW. The dashed line is the relation from Pahl et al. (2021) based on measurements of the LyC from stacks of spectra from galaxies at $z \sim 3$.

on the LyC instead of the adopted 2σ criterion, we find no significant change in the value of τ. We report τ for each of the three f_{esc}^{LyC} indicators ($F_{\lambda LyC}/F_{\lambda 1100}$, f_{esc}^{LyC}(Hβ), and f_{esc}^{LyC}(UV)) in Table 1 for the combined LzLCS and Izotov et al. (2016a, 2016b, 2018a, 2018b, 2021) and Wang et al. (2019) samples. We also report the probability p that the measured τ is consistent with the null hypothesis that f_{esc}^{LyC} is not correlated with the indirect diagnostic. We consider correlations to be significant if $p < 1.350 \times 10^{-3}$ (3σ confidence) and strong if $|\tau| > 0.2$.

Below we examine diagnostics motivated by LyC optical depth and by properties related to stellar feedback mechanisms facilitating LyC escape. Many proxies exhibit an intrinsic, often significant correlation with f_{esc}^{LyC}, but with substantial scatter in the data. This scatter often extends from a parameter-dependent upper bound on f_{esc}^{LyC} down to $f_{esc}^{LyC} = 0$. These upper bounds in f_{esc}^{LyC} suggest that line-of-sight effects (e.g., orientation, covering fraction) may be responsible for obscuring otherwise clear trends, although relationships between various properties may also contribute to the scatter.

To illustrate the combination of obscuring scatter and upper-bound effects, we refer to Figure 1 comparing f_{esc}^{LyC} and $f_{esc}^{Ly\alpha}$. For each of the LyC metrics, the highest f_{esc}^{LyC} values at any given $f_{esc}^{Ly\alpha}$ closely follow the dotted line indicating where $f_{esc}^{LyC} = f_{esc}^{Ly\alpha}$. However, the lowest f_{esc}^{LyC} values at any given $f_{esc}^{Ly\alpha}$ are largely invariant with $f_{esc}^{Ly\alpha}$, consistent with $f_{esc}^{LyC} \approx 10^{-3}$ estimated in the nondetections. Thus, in this example, the identity line $f_{esc}^{LyC} = f_{esc}^{Ly\alpha}$ is an upper bound, or "envelope," to the distribution of f_{esc}^{LyC} values at a particular value of $f_{esc}^{Ly\alpha}$. The envelope represents the intrinsic relationship between f_{esc}^{LyC} and $f_{esc}^{Ly\alpha}$, a trend obscured by the scatter apparent in the observed distribution. Here, this upper bound could originate from a line-of-sight effect. When optically thin regions align with the aperture, $f_{esc}^{LyC} = f_{esc}^{Ly\alpha}$. When optically thin regions are not aligned with the aperture, f_{esc}^{LyC} decreases significantly, while resonant scattering of Lyα photons into the line of sight maintains a high $f_{esc}^{Ly\alpha}$. This upper-bound effect appears in the $f_{esc}^{Ly\alpha}$, [O I], O_{32}, EW Hβ, M_{1500}, β_{1200}, $M_\star$, r_{50}, sSFR, and $12 + \log_{10}$(O/H) diagnostics for at least one of the LyC escape metrics, although the scatter down to $f_{esc}^{LyC} = 0$ tends to be more pronounced in $F_{\lambda LyC}/F_{\lambda 1100}$ and Hβ f_{esc}^{LyC}.

To highlight the intrinsic trends obscured by downward scatter in f_{esc}^{LyC}, we calculate the fraction of galaxies that are prodigious LCEs (LyC detected at $>5\sigma$ and either f_{esc}^{LyC} or $F_{\lambda LyC}/F_{\lambda 1100} > 0.05$) in each diagnostic. This "LCE fraction" indicates the affinity of strong LCEs for certain global properties. Such a preference could be used to select LCEs in future studies.

We define the LCE fraction as the ratio of strong LCEs ($P(>N|B) < 2.867 \times 10^{-7}$ for 5σ significance as in Section 2, and the f_{esc}^{LyC} indicator exceeds 5%) to total galaxies in the combined sample in a given bin of a particular property. Bin counts are given as the sum of the probabilities for the strong LCE and total LCE samples, i.e., the Poisson binomial expected value for each bin. We define the final LCE detection fraction as the ratio of the strong LCE counts to that of the total counts in a given bin. We determine uncertainty in the LCE detection fraction using a Monte Carlo simulation of the ratio of Poisson binomial distributions using 10^4 independent Bernoulli trials for each measurement to determine the distribution of counts in each bin. In cases of upper limits where no uncertainty is reported for a measurement (notably the [O I] line), we follow the root-finding minimization method from Gehrels (1986) to define confidence intervals on the detection fraction. The $F_{\lambda LyC}/F_{\lambda 1100}$ flux ratio tends to agree more with f_{esc}^{LyC}(Hβ) than with f_{esc}^{LyC}(UV); however, f_{esc}^{LyC}(UV) is less dependent on assumptions about stellar populations and star formation history than f_{esc}^{LyC}(Hβ) and contains corrections for dust that are absent in $F_{\lambda LyC}/F_{\lambda 1100}$. Despite some disagreements in values of LCE fraction, f_{esc}^{LyC}, and $F_{\lambda LyC}/F_{\lambda 1100}$, the trend in LCE fraction does not change significantly depending on the f_{esc}^{LyC} indicator.

3.1. Lyα

As both Lyα and the LyC are sensitive to the line of sight, we anticipate the former to trace the LCE fraction rather well, even as the emission line experiences higher optical depths than the continuum for the same column density. We demonstrate that this relation is the case in Figure 2. The LCE fraction increases nearly monotonically with both $f_{esc}^{Ly\alpha}$ and the Lyα EW. Deviations from this trend occur at high $f_{esc}^{Ly\alpha}$ owing to two galaxies having abnormally high Lyα/Hβ ratios corresponding to values of $f_{esc}^{Ly\alpha}$ close to 1.

The overwhelming success of all three Lyα diagnostics in correlating with f_{esc}^{LyC} demonstrates that both Lyα and LyC escape depend on the distribution of neutral hydrogen in a galaxy. While all three are promising candidates for f_{esc}^{LyC} indicators at high redshift, Lyα EW is perhaps the easiest to

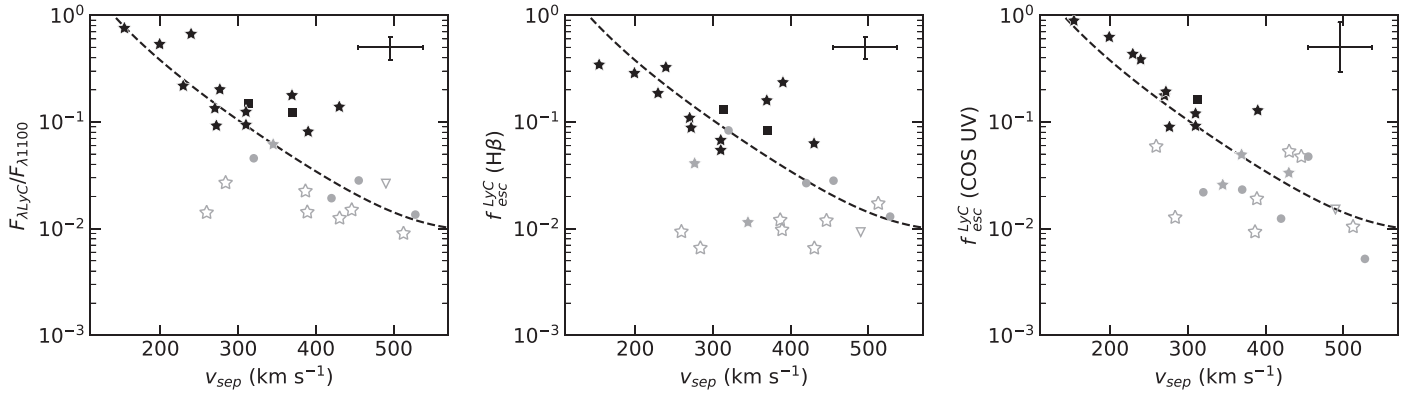

Figure 4. Same as Figure 1, but for Lyα peak velocity separation v_{sep}. Results include only seven galaxies from the LzLCS plus the Izotov et al. (2016a, 2016b, 2018a, 2018b, 2021) samples. The dashed line is the description by Izotov et al. (2018b).

measure, as it requires neither rest-frame optical nor high-resolution spectroscopy. The wealth of Lyα EW measurements of LCEs at higher redshifts ($z \sim 3-4$; e.g., Steidel et al. 2018; Marchi et al. 2018; Fletcher et al. 2019; Pahl et al. 2021) suggests that these diagnostics will likely remain applicable for galaxies at the epoch of reionization. We discuss this possibility in detail in Section 5.3.

3.1.1. Lyα Escape Fraction

In Paper I, we derived $f_{esc}^{Ly\alpha}$ from Lyα and Hβ emission-line fluxes using Case B recombination coefficients determined by the measured electron temperatures and densities. The f_{esc}^{LyC} exhibits a strong correlation with the fraction of escaping Lyα photons. Consistent with previous studies (e.g., Dijkstra et al. 2016; Verhamme et al. 2017; Izotov et al. 2020), we typically find that $f_{esc}^{Ly\alpha} \gtrsim f_{esc}^{LyC}$ and that the envelope of f_{esc}^{LyC} increases with increasing $f_{esc}^{Ly\alpha}$ (Figure 1). This result illustrates that Lyα has an advantage over the LyC in escaping a galaxy because it can resonantly scatter. However, Lyα and LyC escape have a clear physical connection: our results in Figure 1 suggest that only Lyα emitters (LAEs) can be strong LCEs. Indeed, from Figure 1, $f_{esc}^{LyC} = f_{esc}^{Ly\alpha}$ serves as an approximate envelope to the distribution of f_{esc}^{LyC}.

There remains a great deal of scatter in f_{esc}^{LyC} values for any given $f_{esc}^{Ly\alpha}$, which is to be expected. Observed Lyα flux depends on scattering effects from dust and gas along and outside the line of sight, making $f_{esc}^{Ly\alpha}$ sensitive to dust and gas content, ISM clumpiness, and gas dynamics (e.g., Dijkstra et al. 2016). While ISM content and geometry also affect f_{esc}^{LyC}, the scatter evident in Figure 1 suggests that the dependence of f_{esc}^{LyC} on these properties may differ from that of $f_{esc}^{Ly\alpha}$.

3.1.2. Lyα Equivalent Width

In place of $f_{esc}^{Ly\alpha}$, we consider Lyα EW as another possible indicator of f_{esc}^{LyC}. While less directly tracing optical depth than $f_{esc}^{Ly\alpha}$, Lyα EW is far easier to measure at high redshift because, unlike $f_{esc}^{Ly\alpha}$, it does not require observing the Balmer lines. Furthermore, both Henry et al. (2015) and Yang et al. (2017a) demonstrate a strong correlation between $f_{esc}^{Ly\alpha}$ and Lyα EW for Green Peas (GPs).

From Figure 3, f_{esc}^{LyC} is bounded by an upper limit that increases with Lyα EW. We find that the relation between Lyα EW and f_{esc}^{LyC} given by Pahl et al. (2021) provides a reasonable description of this envelope in f_{esc}^{LyC} values up to $\sim$150 Å. Interestingly, this trend extends beyond the 110 Å maximum predicted by Steidel et al. (2018), perhaps due to their assumed continuous star formation history.

The correlation between f_{esc}^{LyC} and Lyα EW is one of the stronger and more significant of the diagnostics we consider, with $\tau \approx 0.3$ across all three f_{esc}^{LyC} indicators. Ten of the 16 galaxies with high Lyα EW are strong leakers, indicating a possible transition in Lyα EW at 100 Å. Galaxies with EWs above this value are far more likely to be strong LCEs than those below it (see also Figure 2). Further supporting this notion of a 100 Å transition, LCEs with EWs below this value are not as prodigious emitters as above it, which may suggest that LCEs with high EW contribute more significantly to the cosmic LyC budget.

Lyα is sensitive to both column density and f_{esc}^{LyC}, which affects the distribution of f_{esc}^{LyC} over the EWs. As the optical depth decreases, more Lyα and LyC photons can escape. The drop in column density will then begin to limit the intrinsic emission of Lyα photons, causing Lyα EW to decrease with increasing f_{esc}^{LyC} (Nakajima & Ouchi 2014; Steidel et al. 2018). This effect may explain why some strong LCEs persist at Lyα EWs at or even below 100 Å. However, Lyα EW also depends very strongly on the continuum flux and, by extension, the stellar population(s), making unclear how significantly f_{esc}^{LyC} affects the Lyα EW. Nevertheless, Lyα EW is still one of the most promising diagnostics for f_{esc}^{LyC}, performing comparably to $f_{esc}^{Ly\alpha}$.

3.1.3. Lyα Peak Velocity Separation

Lyα profiles are typically double peaked, with the velocity separation of the two peaks directly depending on the H I column density (e.g., Verhamme et al. 2015). Previously, Izotov et al. (2018b, 2021) demonstrated that the velocity separation v_{sep} of Lyα peaks strongly correlates with f_{esc}^{LyC} as a result of the strong dependence of both values on the H I column. We compare f_{esc}^{LyC} with v_{sep} for a subset of seven LzLCS galaxies with G160M measurements (Henry et al. 2015; Yang et al. 2017a) and a subset of 20 published LCEs (Verhamme et al. 2017; Izotov et al. 2018b, 2021) in Figure 4. We find a strong relationship between the values. Neither weak leakers nor nondetections persist below $v_{sep} \sim 250$ km s^{-1}

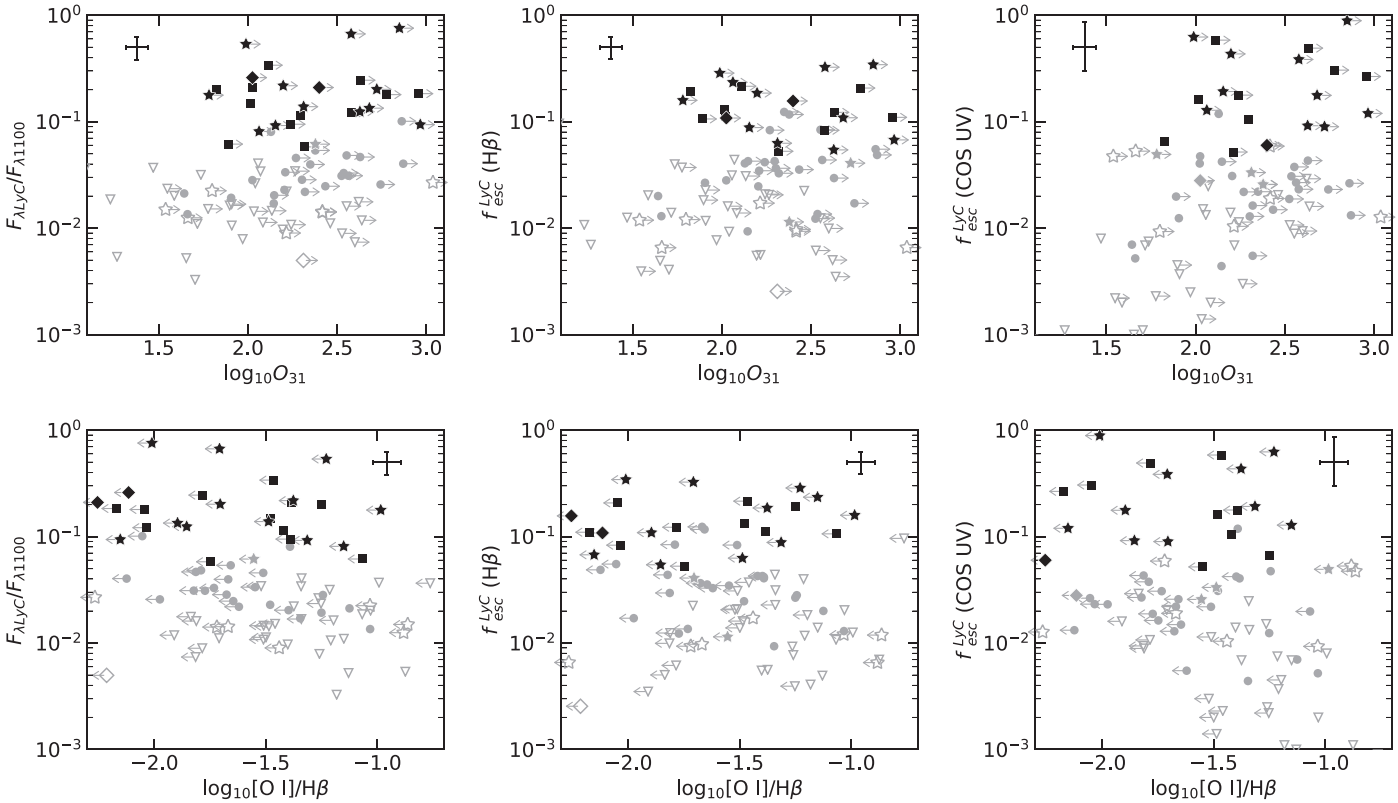

Figure 5. Same as Figure 1, but for O_{31} and [O I]/Hβ.

regardless of f_{esc}^{LyC} metric, which is consistent with predictions by Verhamme et al. (2015). This result favors the H I column density interpretation that motivated this diagnostic.

In Figure 4, we also compare f_{esc}^{LyC} and v_{sep} to the relation from Izotov et al. (2018b) and find that their fit roughly describes the envelope of f_{esc}^{LyC} values. Moreover, we find that v_{sep} has one of the most pronounced correlations of any indirect f_{esc}^{LyC} indicator regardless of f_{esc}^{LyC} metric with $\tau \sim -0.4$. However, additional measurements of v_{sep} from Lyα profiles are necessary to fully test this f_{esc}^{LyC} diagnostic.

3.2. [O I] λ6300

Few of the LCEs have detected [O I] λ6300, with 39 of the 50 LCEs in the combined sample having only upper limits in the emission-line flux, indicating that [O I] may be particularly weak in LCEs (see, however, Plat et al. 2019; Ramambason et al. 2020). The preponderance of [O I] upper limits in LCEs over nonemitters prevents determination of the shape of the distribution of f_{esc}^{LyC} with respect to the [O I] flux ratios, as shown in Figure 5. These upper limits may contribute to the lack of significant correlation (as shown in Table 1, $p > 0.09$ for all three f_{esc}^{LyC} metrics for both [O I] flux ratios).

We compute the [O I] LCE fraction using upper limits when no flux is detected. The LCE fraction distribution (Figure 6) appears relatively monotonic over the [O I] flux ratios O_{31} and [O I]/Hβ. As shown in Figure 6, there is little difference between the three LyC escape indicators. Above $\log_{10} O_{31} \sim 1.8$ and below [O I]/H$\beta \sim -1.3$, the LCE fraction is a roughly constant 30%. The trends with both flux ratios suggest that LCE detection fraction increases with decreasing [O I] flux.

3.3. O_{32}

As shown in Figure 7, we see increasing average and maximum f_{esc}^{LyC} with increasing O_{32}. The total combined sample exhibits a significant ($|\tau| > 0.2$ at $>3\sigma$ confidence) correlation with O_{32} in all three f_{esc}^{LyC} metrics (see Table 1). The f_{esc}^{LyC} relation proposed in Izotov et al. (2018a; dashed line in Figure 7) serves as a description of the envelope in f_{esc}^{LyC} values, particularly in the case of the UV-derived escape fraction (right panel of Figure 7). For the other two f_{esc}^{LyC} metrics, several strong LCEs have f_{esc}^{LyC} in excess of the predicted relation, notably the two LCEs from Wang et al. (2019). These outlying galaxies have higher stellar masses $>10^9$ $M_\odot$, which makes values like $F_{\lambda LyC}/F_{\lambda 1100}$ and f_{esc}^{LyC}(Hβ) more sensitive to the star formation history. Because the majority of the outlying objects exhibit agreement with this envelope when using the UV f_{esc}^{LyC} metric (which assumes a nonparametric star formation history), we interpret these outliers as having f_{esc}^{LyC} systematically biased by this effect rather than evidence that the Izotov et al. (2018b) prescription is not appropriate at low O_{32}.

Scatter of f_{esc}^{LyC} below the envelope could be caused by a number of effects related to line-of-sight optical depth and other galaxy properties. Galaxy-to-galaxy variations in opening angle, covering fraction, burst age, ionization parameter, SFR, metallicity, extinction law and dust, and/or optical depth may indicate that additional physical properties are relevant to determining f_{esc}^{LyC}. Unfortunately, the degenerate dependence of O_{32} on metallicity and ionization parameter substantially complicates any physical interpretation of this result (Sawant et al. 2021). While the mass–metallicity relation appears to evolve with redshift (Sanders et al. 2021), the coupling of 12 + log(O/H) to ionization parameter observed at low

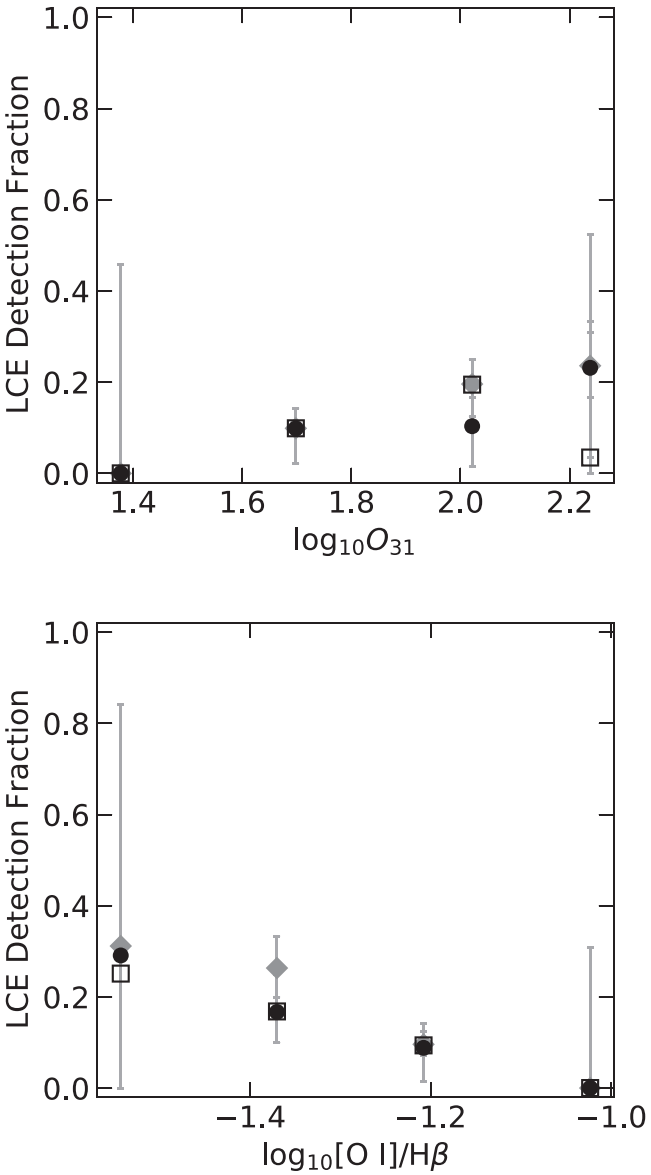

Figure 6. Same as Figure 2, but for O_{31} (top) and [O I]/Hβ (bottom).

redshift persists at $z \sim 2-4$ (Sanders et al. 2020). Therefore, the underlying properties that affect O_{32} remain related in the same way regardless of epoch, supporting the extension of the O_{32} diagnostic to higher redshifts. Regardless of the physical connection between O_{32} and f_{esc}^{LyC}, the scatter in this diagnostic indicates that an isotropic density-bounded escape scenario alone is likely incompatible with the observations. We discuss interpretations and caveats of O_{32} as an f_{esc}^{LyC} diagnostic in greater detail in Sections 4 and 5.

With these nuances to O_{32} in mind, we do find that f_{esc}^{LyC} correlates strongly with O_{32}, particularly for f_{esc}^{LyC} derived from the UV spectrum. Further evidence for this relationship is the LCE fraction shown in Figure 8. The highest-O_{32} galaxies in the combined sample ($O_{32} \gtrsim 10$) have LCE fractions $\gtrsim$0.5. However, LCE fractions >0.1 persist across the full range of O_{32} values regardless of f_{esc}^{LyC} indicator. As we demonstrate in Figure 7, while most galaxies with $O_{32} > 5$ in the combined sample are strong LCEs along the line of sight, some galaxies with lower O_{32} can still be strong LCEs. Two scenarios might contribute to this trend with O_{32}: separate populations of LCEs with LyC escaping under different conditions, or an evolutionary sequence in which LyC escape recurs at later times when fewer early-type stars persist.

3.4. Hβ Equivalent Width

As evident in Figure 9, the average and maximum values of f_{esc}^{LyC} increase with Hβ EW. f_{esc}^{LyC}(UV) has a significant and strong correlation with Hβ EW, indicating at least a moderate relationship between the two. The distribution of f_{esc}^{LyC} appears to occupy two distinct ranges in EW (see also Figure 10), one with high ($\gtrsim$150 Å) EW containing the most prodigious strong LCEs ($f_{esc}^{LyC} \gtrsim 0.1$), and one with low ($\lesssim$150 Å) EW containing additional strong LCEs and the majority of weaker LCEs. Two-thirds of the galaxies in our combined sample with Hβ EW >150 Å have detected LyC. Similarly, 28 of the 39 nondetections appear concentrated at EWs below 150 Å.

Quantifying these results, the fraction of galaxies that are strong LCEs appears to increase with EW, which we demonstrate in Figure 10. This may indicate a preference for young, strong bursts of star formation. As noted above, though, strong LCEs have a wide range in EWs. Thus, the increase in strong LCE fraction with EW demonstrates a dearth of weak LCEs and nonemitters rather than an increase in the prevalence in LCEs at high EW. In other words, high Hβ EW indicates a strong LCE, but high-EW galaxies do not account for the full population of LCEs. Some scatter persists in LCE fraction, particularly at lower EW, depending on the f_{esc}^{LyC} indicator. Uncertainties in the LCE fraction are large enough to suggest that any change in LCE fraction between the various indicators may not be significant. However, our results suggest a significant occurrence of LCEs for EWs below 150 Å, consistent with the f_{esc}^{LyC} trends in Figure 9.

The prevalence of LCEs at high EW demonstrates that Hβ EW is more sensitive to star formation history or sSFR than it is to optical depth. Studies at higher redshifts find similar results in combined Hβ+[O III] EWs (e.g., Castellano et al. 2017; Endsley et al. 2021; Saxena et al. 2022), suggesting that this trend persists in earlier cosmological epochs. As stellar mass and starburst age dominate the Hβ EW, LCEs with high EWs are likely young starbursts and/or low-mass galaxies. The lack of weak LCEs and nonemitters at high EWs may indicate that young ages and/or low masses better facilitate high LyC escape fractions. However, a subset of between 6 and 10 strong LCEs have EWs below 150 Å, indicating that strong LCEs occupy a wide range of ages, star formation histories, and/or sSFRs. These low-EW LCEs are likely more evolved galaxies with higher stellar mass and metallicity. We discuss age and mass further in Section 4.

3.5. FUV Magnitude

The immense scatter in Figure 11 anticipates the weak, insignificant correlation coefficients for observed M_{1500} in all three f_{esc}^{LyC} metrics. Strong leakers persist below $M_{1500} = -20.25$, implying a population of strong LCEs at higher stellar mass or higher UV luminosity. Figure 12 illustrates this persistence of LCEs across a range of M_{1500}. The LCE fraction is relatively constant with observed FUV magnitude, with a slight increase at the faint end of the distribution ($M_{1500} > -19.25$), especially in the UV f_{esc}^{LyC}, where LCEs have $f_{esc}^{LyC} \gtrsim 0.02$ and 9/15 LCEs are strong LCEs. This mild increase may indicate that strong LCEs are

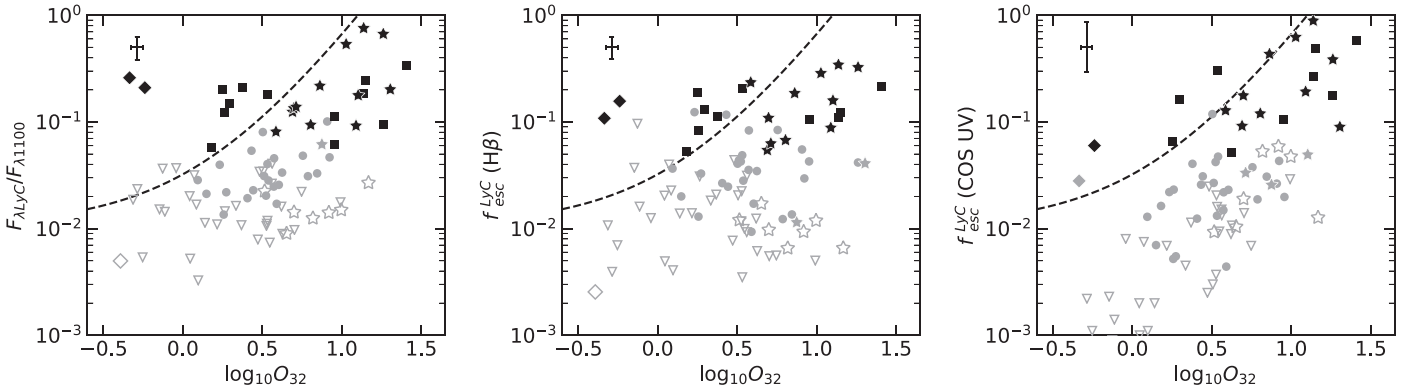

Figure 7. Same as Figure 1, but for the extinction-corrected O_{32} flux ratio. The dashed line indicates the Izotov et al. (2018a) relation. Note that the number of strong LCEs changes depending on the f_{esc}^{LyC} metric.

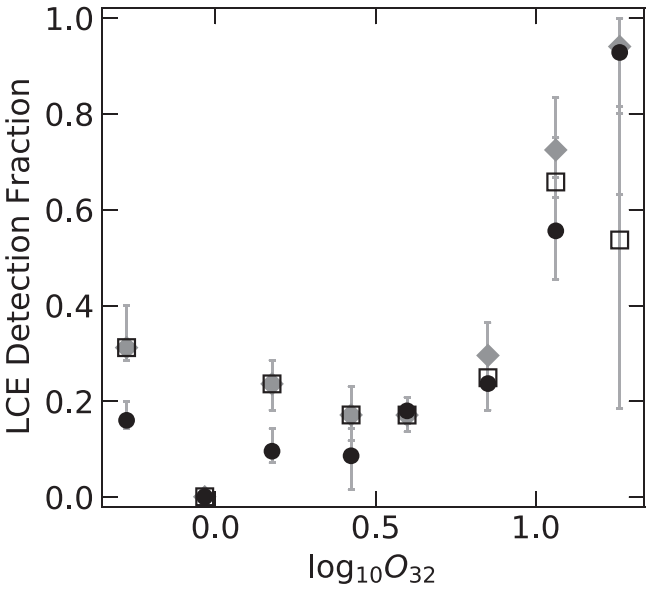

Figure 8. Same as Figure 2, but for O_{32}.

more likely fainter and/or less massive galaxies, particularly given the slight trend in f_{esc}^{LyC} upper bounds with M_{1500}.

The persistence of LCEs at higher UV luminosities could imply that LCEs consist of multiple epochs of recent star formation and/or higher stellar masses. Indeed, EW Hβ declines with increasing UV luminosity such that, for the UV f_{esc}^{LyC}, five of the six strong LCEs and 9 of the 12 weak LCEs with $M_{1500} < -20.25$ have Hβ EWs < 100 Å. A major caveat to this interpretation is the effect of dust on the observed UV magnitude. With the LzLCS, we find that f_{esc}^{LyC} depends on both dust (Saldana-Lopez et al. 2022) and age (Section 3.4), but less so on mass (Section 3.7). Such effects complicate direct interpretation of M_{FUV} as an f_{esc}^{LyC} diagnostic without ancillary information. We discuss M_{1500} in a high-redshift context further in Section 5.3.

3.6. UV β_{1200}

Flury et al. (2022) measured the UV slope β_{1200} from the COS spectra over a range of 1050−1350 Å. While we present results for this measurement below, we note that β_{1200} can be quite different from the commonly used β_{1500}. Therefore, β_{1200} provides only a relative sense of the relationship between β_{1500} and f_{esc}^{LyC}.

Figure 13 demonstrates that the highest f_{esc}^{LyC} values occur for the steepest values of β_{1200}. Indeed, the highest values of f_{esc}^{LyC} all occur where $\beta \leqslant -2$, while a distinct envelope in f_{esc}^{LyC} describes f_{esc}^{LyC} values for $\beta \gtrsim -2$. Though strong LCEs can persist across a wide range of $\beta \in [-3, -1]$, the UV slope has a significant correlation coefficient for two of the three f_{esc}^{LyC} indicators ($\tau \sim -0.25$; see Table 1). As implied by the correlation coefficients and Figure 13, bluer galaxies tend to have higher f_{esc}^{LyC}. The distribution of LCE fraction over UV β_{1200} in Figure 14 is equally informative. LCE fraction increases as the slope steepens from $\sim$0 at $\beta_{1200} > -1$ to nearly 0.6 at $\beta_{1200} \sim -2.5$, suggesting that the strongest LCEs contain young stellar populations without substantial dust attenuation.

These trends in β_{1200} make sense because early-type stars produce the majority of the LyC and low dust extinction better facilitates LyC escape. However, some galaxies with $-2 < \beta < -1$ are strong LCEs, with the Wang et al. (2019) strong LCEs being even redder than -1. One or a combination of scenarios could describe LCEs with $\beta_{1200} > -2$: (i) a patchy dust screen that reddens the UV spectrum but still allows FUV and LyC photons to escape (the so-called "picket fence" model; e.g., Heckman et al. 2001; Saldana-Lopez et al. 2022), and/or (ii) multiple generations of stars that, through feedback processes, facilitate LyC escape by clearing out gas while bolstering the redder part of the UV spectrum with emission from older stellar populations (see discussion in Micheva et al. 2017 of this effect in Mrk 71). We discuss the relationship between β_{1200}, dust, and stellar population age further in Section 4.1.

3.7. Stellar Mass

Simulations disagree as to whether dwarf or more massive star-forming galaxies are the major source of LyC photons for reionization. Figure 15 suggests that dwarf galaxies ($M_\star < 10^9$ $M_\odot$) are more likely to be strong LCEs. More than half (31/52) of the dwarf galaxies in the combined sample are LCEs, 13 of which are strong LCEs.

With increasing mass, the number of strong LCEs and corresponding f_{esc}^{LyC}(UV) values appear to decrease. Even so, galaxies with $M_\star > 10^9$ $M_\odot$ can still be prodigious LCEs, some even having $f_{esc}^{LyC} > 0.1$. The τ coefficient and corresponding p value suggest that the correlation is neither strong nor significant for any f_{esc}^{LyC} metric. Furthermore, the other two f_{esc}^{LyC} metrics do not indicate much of an envelope in f_{esc}^{LyC} with

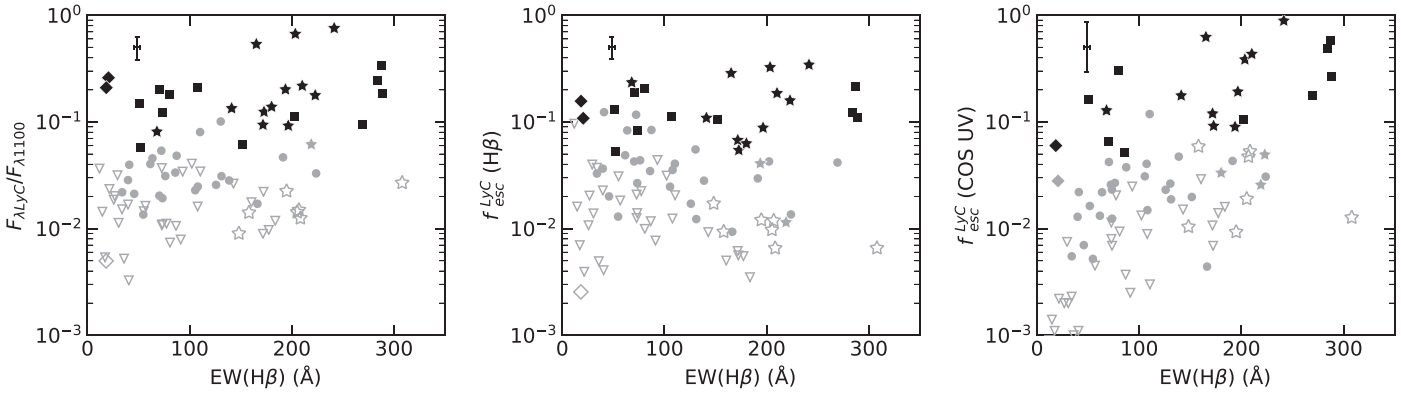

Figure 9. Same as Figure 1, but for the rest-frame Hβ EW.

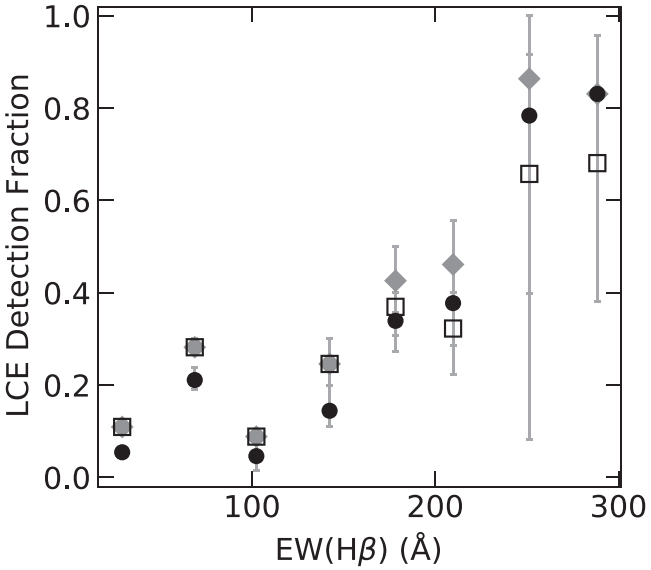

Figure 10. Same as Figure 2, but for rest-frame EW(Hβ).

$M_\star$. As evident in Figure 16, the LCE fraction distribution is also relatively flat over the range of stellar masses. Like M_{1500}, the distribution of $f_{\rm esc}^{\rm LyC}$ with respect to $M_\star$ suffers from substantial scatter. Unlike M_{1500}, the stellar masses have relatively large uncertainties. These large uncertainties may contribute to the apparent scatter and even to the flat LCE fraction distribution.

3.8. Σ_{SFR}, sSFR, and Half-light Radius

$\Sigma_{\rm SFR}$ exhibits a threshold of $\Sigma_{\rm SFR} \sim 10\ M_\odot\ {\rm yr}^{-1}\,{\rm kpc}^{-2}$ above which nearly all strong LCEs appear, as evidenced by Figure 17. We see scatter in $f_{\rm esc}^{\rm LyC}$ similar to other diagnostics examined here, again implying the effects of orientation or variations in host galaxy properties. For comparison, we also show $f_{\rm esc}^{\rm LyC}$ as it varies with half-light radius in Figure 17. The prominent transition in $f_{\rm esc}^{\rm LyC}$ at $r_{50} \approx 0.7$ kpc suggests that the concentration of star formation dominates $\Sigma_{\rm SFR}$ in strong LCEs.

This affinity of strong LCEs for high $\Sigma_{\rm SFR}$ and low r_{50} suggests that higher concentrations of star formation provide the feedback necessary to clear LyC escape paths in the ISM. Consistent with this interpretation, we find that the maximum observed value of $f_{\rm esc}^{\rm LyC}$ increases with sSFR. Although less pronounced, this envelope in $f_{\rm esc}^{\rm LyC}$ is similar to the $f_{\rm esc}^{\rm LyC} \propto \Sigma_{\rm SFR}^{0.4}$ relation described by Naidu et al. (2020). These trends suggest that concentrated star formation may be a good indicator of $f_{\rm esc}^{\rm LyC}$ and could be pivotal to understanding the origin of reionization.

We show the LCE fraction with respect to both $\Sigma_{\rm SFR}$ and sSFR in Figure 18. In both cases, LCE fraction clearly increases with the concentration of star formation. The LCE fraction changes relatively little with $\Sigma_{\rm SFR}$ until reaching $\approx$10 $M_\odot\,{\rm yr}^{-1}\,{\rm kpc}^{-2}$, at which point LCE fraction increases from $\sim$10% to 60% over half a decade in $\Sigma_{\rm SFR}$. LCE fraction increases more gradually with sSFR, suggesting that the concentration of star formation is more important than the effects of stellar mass.

Comparing $\Sigma_{\rm SFR}$, sSFR, and $\Sigma_{\rm sSFR} = \Sigma_{\rm SFR}/M_\star$ highlights this point, as $\Sigma_{\rm SFR}$ and $\Sigma_{\rm sSFR}$ yield much higher τ values than sSFR. The τ values of $\Sigma_{\rm SFR}$ and $\Sigma_{\rm sSFR}$ are also quite comparable, which demonstrates that factoring in stellar mass does not produce a better diagnostic. This result comes with the caveat that the LzLCS stellar masses have high uncertainties, which could mitigate any effects stellar mass may have on the observed trends.

High $\Sigma_{\rm SFR}$, like those seen for GP galaxies, need not imply unusually strong SN feedback (e.g., Chisholm et al. 2017; Jaskot et al. 2017). Because $\Sigma_{\rm SFR}$ is derived from Hβ, the apparent envelope in $f_{\rm esc}^{\rm LyC}$ could instead arise from an increased compactness of H II regions. Indeed, τ is higher and more significant for r_{50} than for $\Sigma_{\rm SFR}$, sSFR, or $\Sigma_{\rm sSFR}$. Such concentrated star-forming regions could deplete the surrounding gas so that LyC photons can leave the local H II region and escape into the more diffuse host galaxy and potentially escape into the IGM.

3.9. Metallicity

In Figure 19, we compare $f_{\rm esc}^{\rm LyC}$ to the gas-phase metallicity $12 + \log_{10}({\rm O/H})$. The LCEs with $f_{\rm esc}^{\rm LyC} \gtrsim 10\%$ all reside below $12 + \log_{10}({\rm O/H}) \sim 8.1$. Much like the case of $M_\star$, the strong LCEs with $f_{\rm esc}^{\rm LyC} \lesssim 10\%$ and the weak LCEs are more evenly distributed from $12 + \log_{10}({\rm O/H}) = 7.7$ to 8.5. While substantial scatter appears in all three diagnostics, roughly two-thirds (28/39) of the non-LCEs fall *above* $12 + \log_{10}({\rm O/H}) \sim 8.1$. With a correlation coefficient of $\tau \sim -0.2$ at about 2σ significance, $f_{\rm esc}^{\rm LyC}$ does not have a significantly strong correlation with $12 + \log_{10}({\rm O/H})$; however, the preferences of the most prodigious LCEs for lower

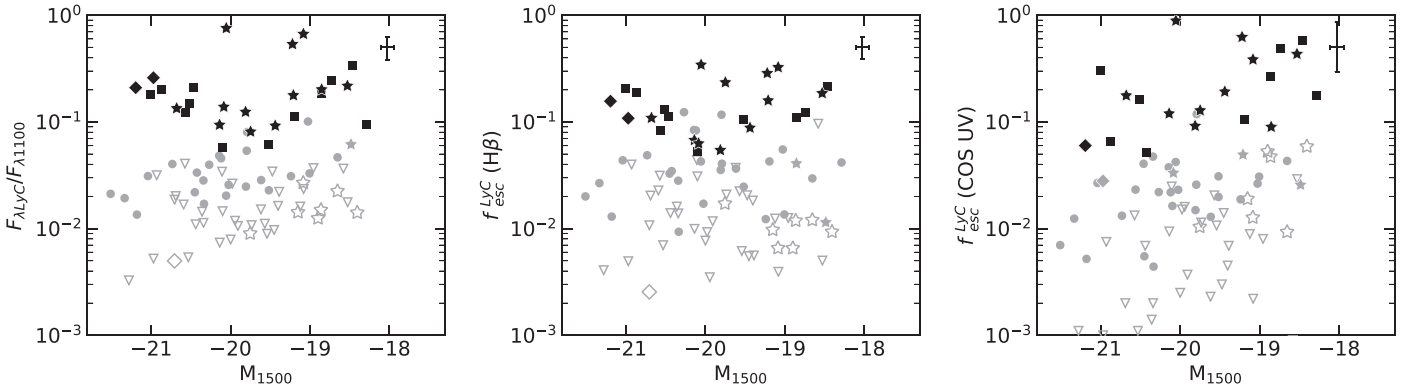

Figure 11. Same as Figure 1, but for M_{1500}.

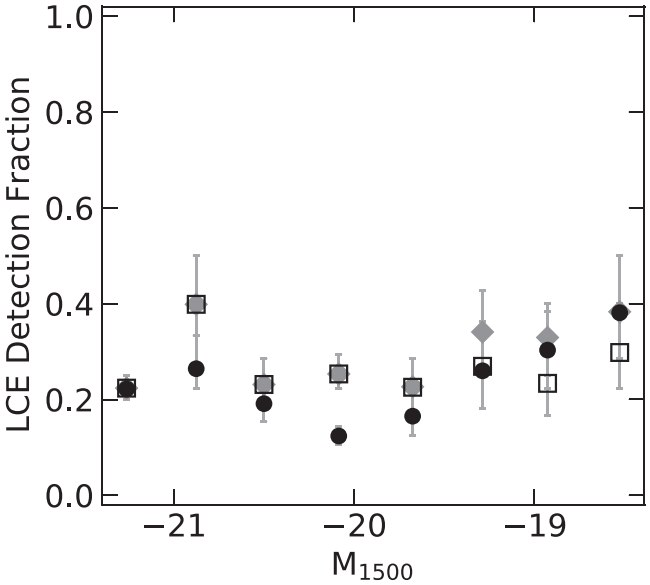

Figure 12. Same as Figure 2, but for M_{1500}.

metallicities and non-LCEs for higher metallicities are promising as a diagnostic.

The LCE fraction shown in Figure 20 also suggests that $12 + \log_{10}(\mathrm{O/H})$ is a promising, albeit complicated, diagnostic. As with the f_{esc}^{LyC} trends shown in Figure 19, we see strong LCEs both above and below $12 + \log_{10}(\mathrm{O/H}) \sim 8.1$. Given the uncertainty in the LCE fraction, it is unclear whether the lack of LCEs at intermediate values of $12 + \log_{10}(\mathrm{O/H}) \sim 8.1$ implies the existence of distinct LCE populations separated by metallicity.

3.10. Summary of Correlations

Ten of the 17 indirect f_{esc}^{LyC} diagnostics considered above are significantly strong ($|\tau| > 0.2$ with $p < 0.00135$, 3σ significance): $f_{esc}^{Ly\alpha}$, EW Lyα, v_{sep}, O_{32}, EW Hβ, β_{1200}, $M_{1500,int}$, NUV r_{50}, Σ_{SFR}, and Σ_{sSFR}. The $f_{esc}^{Ly\alpha}$, EW Lyα, β_{1200}, NUV r_{50}, and Σ_{SFR} diagnostics are significantly strong across both f_{esc}^{LyC} metrics. These five diagnostics are thus the most compelling for identifying LCEs and inferring f_{esc}^{LyC}. Hβ EW and $M_{1500,int}$ are significantly strong correlations only with the COS UV f_{esc}^{LyC}. In general, f_{esc}^{LyC} derived from fitting the UV spectrum gives the strongest, most significant correlations for nearly all the indirect diagnostics. The success of this particular LyC escape indicator is particularly compelling because, as discussed in Section 2, it is the most reliable and direct measure of f_{esc}^{LyC}.

The indirect f_{esc}^{LyC} diagnostics motivated by optical depth contain the majority of the strong correlations. Likely owing to their unique sensitivity to H I, the diagnostics based on Lyα—$f_{esc}^{Ly\alpha}$, Lyα EW, and profile peak separation—have the strongest correlations as measured by Kendall's τ for censored data. However, the v_{sep} correlations lack the significance of the other Lyα correlations, in part because of insufficient data. While not as strongly correlated with f_{esc}^{LyC} as the Lyα properties, the O_{32} flux ratio still exhibits a strong, significant correlation. The [O I] flux relative to other emission lines' is less successful as an f_{esc}^{LyC} diagnostic, likely owing to the faintness of [O I].

Of the remaining diagnostics, which are motivated by the physical mechanism behind LyC escape, the half-light radius and Σ_{SFR} have the strongest, most significant correlations with f_{esc}^{LyC}. Indeed, strong LCEs exhibit clear associations with highly concentrated star formation, distinguishing which sorts of galaxies or regions within galaxies are emitting LyC. Both Hβ EW and UV β_{1200} also correlate strongly and significantly with f_{esc}^{LyC}. While stellar mass and attenuated UV magnitude lack strong, significant correlations, these two diagnostics still exhibit envelopes in f_{esc}^{LyC} and suggest that the strongest LCEs have $M_\star < 10^9\ M_\odot$. Such envelopes in f_{esc}^{LyC} indicate that multiple properties contribute to an ideal escape scenario, including starburst age, ionization parameter, SFR, and orientation of optically thin channels.

4. Relationships between Diagnostics

The results of these indirect diagnostics, particularly the envelopes in f_{esc}^{LyC}, prompt further investigation of two-dimensional diagnostics to determine trends in f_{esc}^{LyC} with multiple parameters and explore sources of the scatter apparent in many diagnostics. Below, we consider relationships between diagnostics regarding stellar population age (β_{1200} vs. Hβ EW, O_{32} vs. Hβ EW), star formation history (O_{32} vs. $M_\star$, O_{32} vs. $12 + \log_{10}(\mathrm{O/H})$), ionization structure (O_{32} vs. O_{31}), and ionization versus mechanical feedback (Σ_{SFR} vs. O_{32}). Given fewer systematic uncertainties associated with the UV SED f_{esc}^{LyC}, we proceed with this particular f_{esc}^{LyC} metric in our subsequent analysis and discussion.

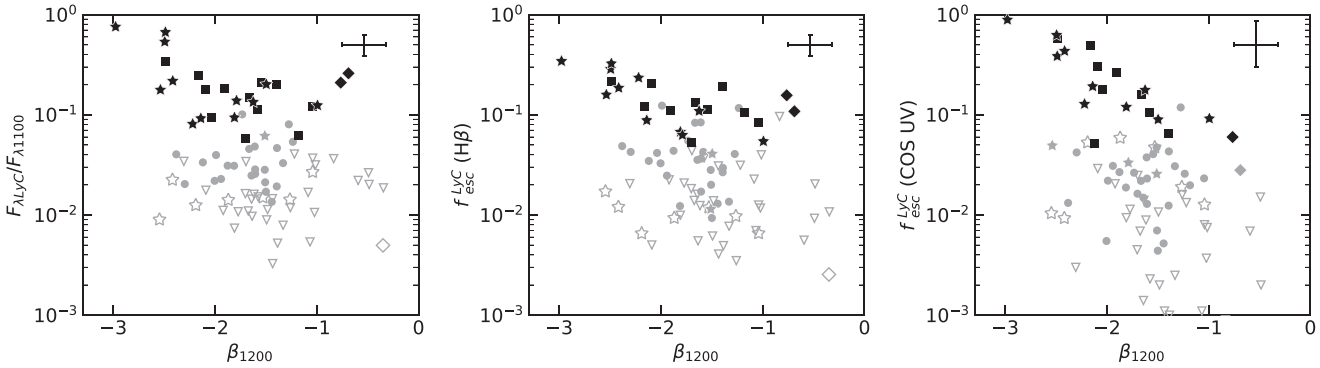

Figure 13. Same as Figure 1, but for the UV spectral index β_{1200}.

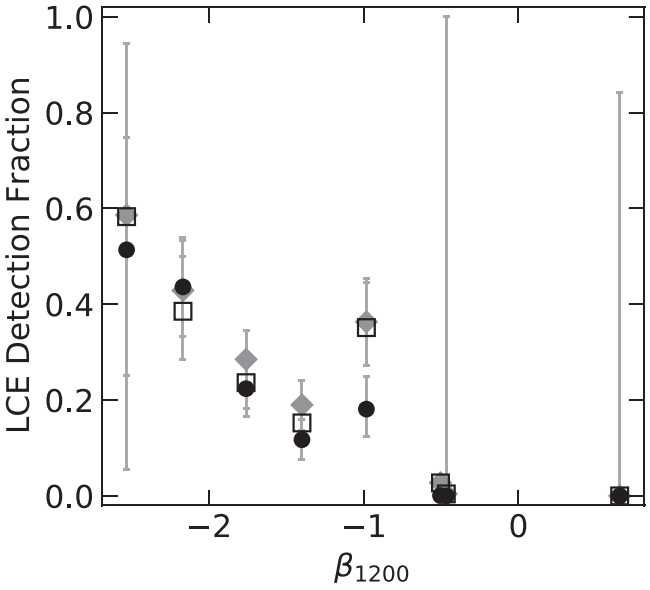

Figure 14. Same as Figure 2, but for UV β_{1200}.

4.1. UV β_{1200} versus Hβ EW

Although most galaxies with Hβ EWs < 150 Å do not appear to be associated with LyC escape (Section 3.4), Zackrisson et al. (2013) propose that the UV β_{1200}–Hβ EW plane could constrain f_{esc}^{LyC}. We compare their model predictions for $f_{esc}^{LyC} = 0.0$, 0.5, and 0.9 to the LzLCS results in Figure 21 for ∼30% solar-metallicity picket fence nebulae over a range of 10^6–7×10^8 yr burst ages. Our combined results do not agree with their predictions. We do see a mild gradient in f_{esc}^{LyC} over UV β_{1200} that appears to shift to steeper continua with increasing EW, as their predictions suggest. However, the observed locus appears shifted to higher spectral slopes: only one previously published LCE falls into the $f_{esc}^{LyC} > 0$ space predicted by Zackrisson et al. (2013).

A major caveat to this apparent disagreement is the effect of dust, which may substantially affect the predicted sequences in the UV β_{1200}–Hβ EW plane (Zackrisson et al. 2017). Moreover, the star formation history also determines where a galaxy resides in Figure 21, as underlying older stellar populations can strongly affect the optical continuum and thus the Hβ EW. LzLCS galaxies appear to be older and/or dustier than the Zackrisson et al. (2013) models, which places our sample at lower Hβ EW and higher UV β_{1200} than their predictions. Interpreting the discrepancy comes with an additional complication that the UV β predicted in Zackrisson et al. (2013) is measured at redder wavelengths than those accessible in the COS spectrum. Because an attenuated young stellar SED peaks at ∼1100–1200 Å, β_{1200} is necessarily different from the Zackrisson et al. (2013) UV β predictions. That being said, we find no distinguishable trends in f_{esc}^{LyC} in the β_{1200}–EW(Hβ) plane.

Whereas the Zackrisson et al. (2013) models suggest that strong LCEs should have low Hβ EWs and low UV β_{1200}, the strongest LCEs have high (>100 Å) Hβ EWs, while those LCEs with lower EWs have higher UV β_{1200}. The latter group of LCEs may contain porous H II regions with optically thin channels cleared by SN feedback or turbulence (see Section 5). In particular, a two-stage starburst or dusty young starburst could be responsible for the high UV β_{1200}, low Hβ EW exhibited by some of the strong LCEs.

4.2. O_{32}: Age, Mass, Metallicity

Starburst age and ionization parameter are related since the earliest O stars die off within the first 2–4 million years. Because these stars dominate the LyC flux, properties sensitive to ionization parameter like O_{32} will consequently depend, at least in part, on the age of the starburst (e.g., Jaskot & Oey 2013; Izotov et al. 2017), in addition to other properties. Figure 22 demonstrates a tight relationship between O_{32} and Hβ EW.

The trend in Figure 22 could result from a variety of processes. Decreasing Hβ flux due to fewer ionizing photons would decrease the EW in tandem with O_{32} as the O^{+2} zone declines relative to O^{+}. Due to the mass–metallicity correlation for galaxies (e.g., Tremonti et al. 2004), increased continuum flux due to higher galaxy mass would decrease the EW while increasing the metallicity, the latter serving to decrease O_{32}. We find that O_{32} and EW decrease with increasing mass, but because mass correlates with $12 + \log_{10}(O/H)$, it is not clear whether mass dominates this trend.

We find that LCEs occupy a wide range in O_{32} and Hβ EW. Roughly half of the LCEs occur at $\log_{10} O_{32} > 1$ or Hβ EW > 100 Å. Nonemitters do not appear in this part of the diagram, while all the $f_{esc}^{LyC} > 0.2$ leakers reside here. The remaining LCEs have lower Hβ EWs (≈50–150 Å), where many of the nonemitters also reside. These separate sets of LCEs may imply different starburst ages or stellar mass populations at which LyC escape occurs.

Escaping LyC photons should affect both Hβ EW and O_{32}. The former should decrease owing to a drop in Hβ flux, while the latter should increase owing to a drop in [O II] flux. A lack

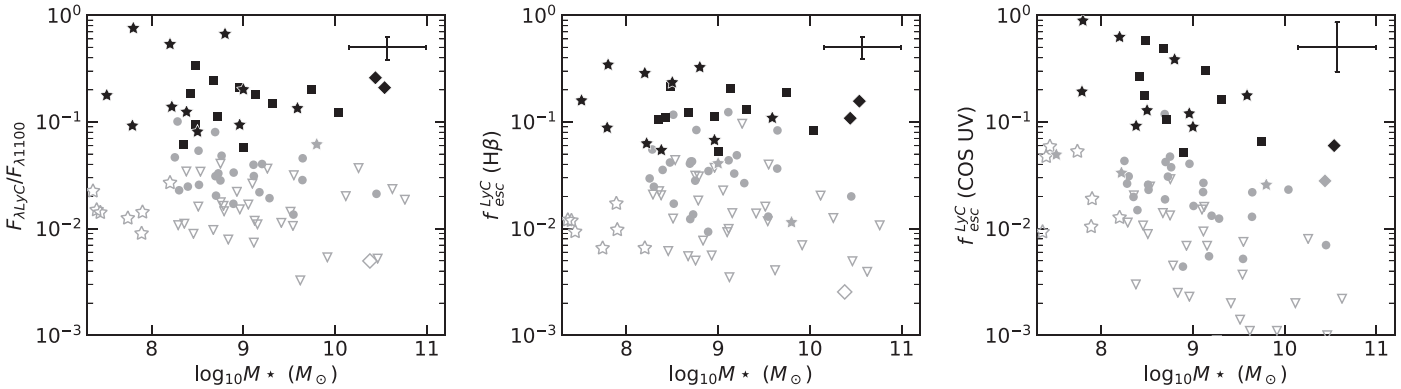

Figure 15. Same as Figure 1, but for stellar mass.

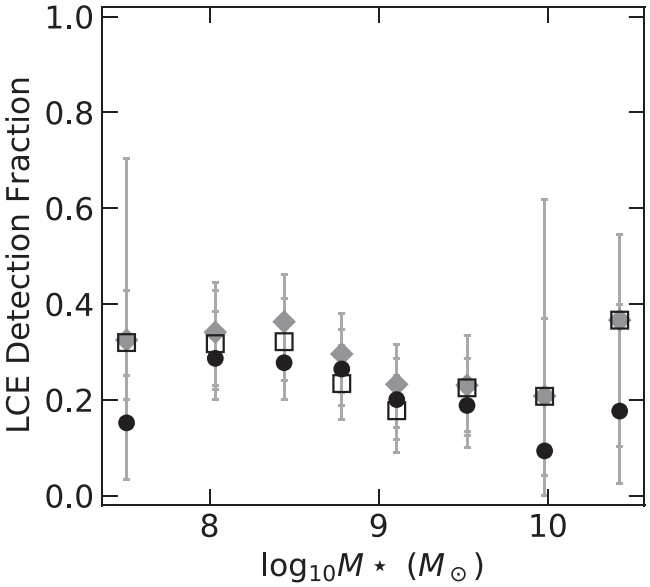

Figure 16. Same as Figure 2, but for $M_\star$.

of preference of f_{esc}^{LyC} for any part of the distribution demonstrates that age and ionization parameter mitigate any effects of escaping LyC photons on the measured properties.

Gas-phase and stellar metallicities also affect O_{32}. As collisionally excited lines, [O III] and [O II] depend on electron temperature, which is higher in low-metallicity gas owing to decreased cooling by metal emission lines. Higher stellar metallicity changes the opacity of stellar interiors and thus affects their photosphere temperatures. Secondarily, high stellar metallicity increases line blanketing in the LyC of O and B stars. These metallicity effects on stellar atmospheres serve to decrease the ionizing photon budget. These dependencies on gas-phase and stellar metallicity indicate that O_{32} correlates with an abundance indicator like $12 + \log_{10}(O/H)$, which we show in Figure 23.

While there is some scatter, a trend persists between O_{32} and $12 + \log_{10}(O/H)$ over nearly an entire decade. Although high f_{esc}^{LyC} LCEs tend to have higher O_{32} and lower $12 + \log_{10}(O/H)$, LCEs populate the majority of the distribution in Figure 23. Harder ionizing spectra at lower metallicity could facilitate a density-bounded escape scenario. Weaker feedback from low-metallicity stars may also generate a dense, clumpy gas geometry that enables LyC escape (Jaskot et al. 2019), perhaps owing to low covering fractions (e.g., Gazagnes et al. 2020; Saldana-Lopez et al. 2022). Mechanical feedback from stars is stronger at higher metallicity, which might explain the subpopulation of high LCEs at higher metallicity. However, higher metallicity is also linked to higher UV attenuation (e.g., Wang et al. 2019), thereby limiting LyC escape. The reduced f_{esc}^{LyC} of LCEs at higher metallicity may also be due to the fact that, at higher galaxy masses, increased gravity may reduce the effectiveness of feedback and thus limit LyC escape.

Following the known mass–metallicity relation, O_{32} ought to anticorrelate with $M_\star$ just as it does with $12 + \log_{10}(O/H)$. Indeed, in Figure 23 we see such a trend until $M_\star \lesssim 10^9\ M_\odot$ (corresponding to $O_{32} \approx 2$–3), at which point the two properties appear to decouple. With weaker gravitational potentials, low-$M_\star$ galaxies also undergo more bursty star formation (e.g., Weisz et al. 2012; Guo et al. 2016). Such episodic star formation results in a range of stellar feedback and ionization parameters, which would lead to a wide range in O_{32}.

For a given metallicity or stellar mass, strong LCEs tend to have the highest O_{32} values. The leakers with $f_{esc}^{LyC} > 0.2$ concentrate at low $12 + \log_{10}(O/H)$, low $M_\star$, and high O_{32}. Thus, the strength of a starburst relative to the mass of a galaxy may determine its likelihood of leaking LyC.

4.3. Oxygen Ionization Structure

Photoionization models predict that O_{31} should increase by 0.5 dex or more as the LyC optical depth decreases from ionization to density boundary conditions at a fixed O_{32} (e.g., Stasińska et al. 2015; Plat et al. 2019; Ramambason et al. 2020). We compare our results to the predicted sequences for radiation- and density-bounded nebula models from Stasińska et al. (2015) in Figure 24. The combined samples reside on or above the radiation-bounded sequence. We find no relationship between f_{esc}^{LyC} and any offset from the locus. Because the strongest LCEs have only upper limits in [O I], these galaxies may in fact be consistent with density-bounded or picket fence scenarios. LCEs with detected [O I] reside along the radiation-bounded model predictions, which may suggest that an isotropic density-bounded escape scenario is not realized. Indeed, Ramambason et al. (2020) predict that density-bounded channels within an otherwise optically thick medium can describe the distribution of O_{32} and O_{31} flux ratios we observe for LCEs with $f_{esc}^{LyC} \lesssim 0.1$. The [O I] flux from LCEs with high O_{32} and disproportionately low O_{31} may also be contaminated by shocks, causing O_{31} to shift to lower values than other LCEs (Stasińska et al. 2015; Plat et al. 2019).

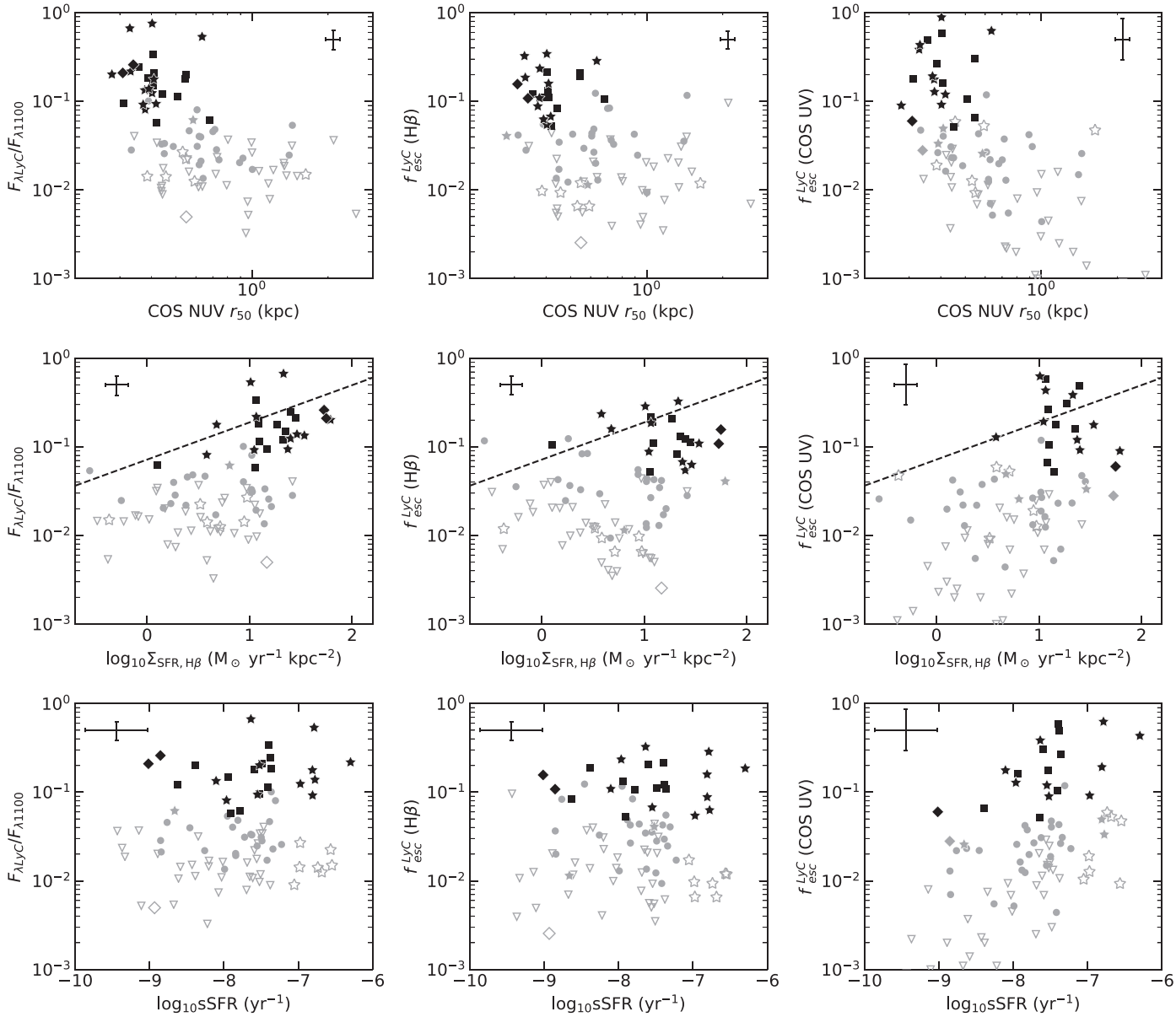

Figure 17. Same as Figure 1, but for UV half-light radius r_{50}, Σ_{SFR}, and sSFR. The dashed line in Σ_{SFR} is the $f_{esc}^{LyC} \propto \Sigma_{SFR}^{0.4}$ relation from Naidu et al. (2020).

4.4. Σ_{SFR}: Ionization and Age

Σ_{SFR} describes the concentration of O and B stars. As a result, Σ_{SFR} influences the ionization parameter, which depends strongly on the number density of early-type stars. At least in the case of density-bounded LyC escape, we anticipate higher O_{32} for LCEs than for nonemitters of the same Σ_{SFR} owing to a deficit in [O II] flux.

We find that LCEs prefer high Σ_{SFR} and high O_{32}, although only one of the two is necessary to demonstrate the likelihood of LyC escape. Figure 25 demonstrates that, with few exceptions, LCEs have high O_{32}, high Σ_{SFR}, or a combination thereof. The LCE population with $\log_{10}\Sigma_{SFR} < 1$ $M_\odot$ yr^{-1} kpc^{-2} is sparse. Thus, high O_{32} and high Σ_{SFR} are each indicative of LCEs, in particular *strong* LCEs, with the most extreme LCEs having both high O_{32} and high Σ_{SFR}.

Combined with the results of UV β_{1200} and Hβ EW, the combination of Σ_{SFR} and O_{32} could suggest two different types of strongly star-forming LCEs. One population is younger with high O_{32}, high Hβ EW, and low metallicity. The other population has lower O_{32}, lower Hβ EW, and higher metallicity and resides in the upper left corner of Figure 25. The latter suggests mechanical feedback, while the former population may point to the additional role of ionization.

5. Discussion

5.1. Insight into Lyman Continuum Escape

The substantial scatter evident in all considered diagnostics could be attributed to one or both of two physical explanations. First, orientation could cause the observed scatter since f_{esc}^{LyC} likely depends on line of sight in an anisotropic, radiation-bounded escape scenario (e.g., Zastrow et al. 2013; Cen & Kimm 2015). Alternatively, the observed scatter might be due to a time delay between the onset of star formation and the escape of the LyC since feedback requires sufficient time to clear out escape channels, thus decoupling properties from f_{esc}^{LyC} to some extent (e.g., Trebitsch et al. 2017; Barrow et al.

Table 1

Kendall τ Correlation Coefficients for Proposed LyC $f_{\rm esc}^{\rm LyC}$ Diagnostics for the Combined LzLCS and Izotov et al. (2016a, 2016b, 2018a, 2018b, 2021) and Wang et al. (2019) Sample, Accounting for Upper Limits in $F_{\lambda \rm LyC}/F_{\lambda 1100}$ and $f_{\rm esc}^{\rm LyC}$ following Akritas & Siebert (1996)

Diagnostic	$F_{\lambda \rm LyC}/F_{\lambda 1100}$			$f_{\rm esc}^{\rm LyC}(\rm H\beta)$			$f_{\rm esc}^{\rm LyC}(\rm UV)$		
	τ	p	σ	τ	p	σ	τ	p	σ
$f_{\rm esc}^{\rm Ly\alpha}$	0.292	5.186×10^{-5}	3.882	0.343	1.942×10^{-6}	4.618	0.324	6.774×10^{-6}	4.351
EW(Lyα)	0.320	8.687×10^{-6}	4.296	0.234	1.141×10^{-3}	3.051	0.342	2.011×10^{-6}	4.610
$v_{\rm sep}$	−0.493	3.103×10^{-4}	3.422	−0.422	2.033×10^{-3}	2.873	−0.530	1.055×10^{-4}	3.705
$\log_{10}\rm O_{31}$	−0.149	0.039	1.761	−0.144	0.045	1.693	−0.151	0.036	1.796
$\log_{10}$[O I]/Hβ	−0.148	0.041	1.745	−0.145	0.044	1.709	−0.145	0.044	1.705
$\log_{10}\rm O_{32}$	0.290	5.678×10^{-5}	3.860	0.198	6.024×10^{-3}	2.511	0.347	1.438×10^{-6}	4.679
EW(Hβ)	0.223	1.953×10^{-3}	2.886	0.109	0.132	1.117	0.283	8.366×10^{-5}	3.764
$M_{\rm 1500,obs}$	0.045	0.533	0.000	−0.013	0.857	0.000	0.098	0.174	0.940
$M_{\rm 1500,int}$	0.228	1.591×10^{-3}	2.950	0.157	0.029	1.895	0.320	8.978×10^{-6}	4.289
β_{1200}	−0.221	2.200×10^{-3}	2.848	−0.261	2.966×10^{-4}	3.435	−0.283	8.366×10^{-5}	3.764
$\log_{10} M\star$	−0.089	0.216	0.785	−0.074	0.307	0.503	−0.167	0.021	2.040
COS NUV r_{50}	−0.388	7.179×10^{-8}	5.261	−0.301	2.938×10^{-5}	4.018	−0.382	1.193×10^{-7}	5.166
$\log_{10}\Sigma_{\rm SFR,H\beta}$	0.368	3.884×10^{-7}	4.941	0.264	2.650×10^{-4}	3.465	0.325	7.099×10^{-6}	4.341
$\log_{10}\Sigma_{\rm SFR,F\lambda 1100}$	0.070	0.334	0.429	0.068	0.347	0.394	−0.035	0.632	0.000
$\log_{10}$sSFR	0.110	0.128	1.138	0.043	0.554	0.000	0.181	0.012	2.254
$\log_{10}\Sigma_{\rm sSFR,H\beta}$	0.290	6.320×10^{-5}	3.833	0.208	4.167×10^{-3}	2.638	0.346	1.859×10^{-6}	4.627
$12 + \log_{10}\left(\frac{\rm O}{\rm H}\right)$	−0.187	9.484×10^{-3}	2.346	−0.130	0.070	1.475	−0.211	3.420×10^{-3}	2.705

Note. p values indicate the false-positive probability that the correlation is real. σ values, given by probit$(1-p)$, indicate the significance of the correlation, i.e., the number of standard deviations separating the correlation statistic from that of the null hypothesis. The characteristic 1σ uncertainties in τ estimated by bootstrapping values of the $f_{\rm esc}^{\rm LyC}$ metrics and indirect diagnostics are ± 0.05. Each correlation is assessed using all 89 objects in the combined LzLCS sample except $v_{\rm sep}$, which is only measured for 7 LzLCS and 20 published objects.

2020; Naidu et al. 2022). Whatever might cause this scatter, it is likely physical because an upper envelope in $f_{\rm esc}^{\rm LyC}$ persists across several diagnostics. These envelopes suggest that genuine trends do exist between $f_{\rm esc}^{\rm LyC}$ and different parameters, but orientation, time delays, and/or starburst properties like age and ionization parameter might influence the values of $f_{\rm esc}^{\rm LyC}$, causing the observed scatter.

As implied by the envelopes and correlations in the $f_{\rm esc}^{\rm LyC}$ diagnostics, the strongest correlations are Lyα EW, $f_{\rm esc}^{\rm Ly\alpha}$, and $v_{\rm sep}$ for the diagnostics motivated primarily by optical depth. Other diagnostics with strong correlations include $\rm O_{32}$, Hβ EW, $\Sigma_{\rm SFR}$, and r_{50}, which may give insights into the physical mechanisms responsible for LyC escape. Some properties, notably $\rm O_{32}$ and Hβ EW, exhibit a broad range in galaxies with $f_{\rm esc}^{\rm LyC} > 0.05$. Different LyC escape scenarios (e.g., Kakiichi & Gronke 2021; Gazagnes et al. 2020) could populate different parts of these diagnostics because the corresponding conditions (e.g., optical depth, porosity of the ISM, or feedback mechanism driving LyC escape) correspond to different ranges of the observable parameter space of $\rm O_{32}$ and Hβ EW.

Investigation of two-dimensional diagnostics sheds light on these possible explanations. At higher mass and higher metallicity, the lower $\rm O_{32}$, lower Hβ EW LCEs likely clear out their birth cloud by mechanical feedback from early-type stars. This serves to more uniformly distribute the dense gas and dust leftover from star formation into an optically thick bubble around the O and B stars. SN feedback and turbulent feedback subsequently clear optically thin channels in this bubble.

The younger, lower-mass, lower-metallicity nature of the high $\rm O_{32}$, high Hβ EW LCEs indicates that this second class of LyC leakers are like the GP galaxies. Such galaxies, while strongly star-forming, likely lack the high-velocity outflows necessary to expel the remnant birth cloud material and form a uniform obscuring medium (Jaskot et al. 2019). However, they may have sufficient radiative feedback to evacuate cavities in the ISM (Kakiichi & Gronke 2021). As a result, these GP LCEs might contain an ISM that is optically thin except where dense clouds cause optically thick patches of relatively small covering fractions. We speculate that the range of parameter spaces occupied by LCEs indicates a shift in conditions and escape mechanism from young GP starbursts with large optically thin cavities to older, optically thick star-forming galaxies with a porous ISM.

While these putative differences in LCEs spurred our comparison of $f_{\rm esc}^{\rm LyC}$ proxies, the two-dimensional diagnostics also demonstrate how different parameters depend on one another. These comparisons show that metallicity, mass, $\Sigma_{\rm SFR}$, age, and ionization parameter are inextricably linked. Furthermore, we find that age and ionization parameter dominate any optical depth effects on properties like $\rm O_{32}$ and Hβ EW. In other words, young ages and strong radiation boost $\rm O_{32}$ and Hβ EW in the strongest LCEs and may be critical for high levels of LyC escape. It is also plausible that a feedback-induced time delay introduces LCE "stragglers" into the distributions of $f_{\rm esc}^{\rm LyC}$ (e.g., Trebitsch et al. 2017; Secunda et al. 2020).

5.2. Comparison with Simulations

Cosmological simulations provide a critical link between the low-redshift LCEs and high-redshift surveys. Predictions from simulations connect parameters such as stellar mass and $\Sigma_{\rm SFR}$ to $f_{\rm esc}^{\rm LyC}$ at the epoch of reionization. Because LzLCs galaxies and other GP-like galaxies are reasonable analogs of high-redshift galaxies, comparing our results to these predictions from simulations can be useful both for translating indirect

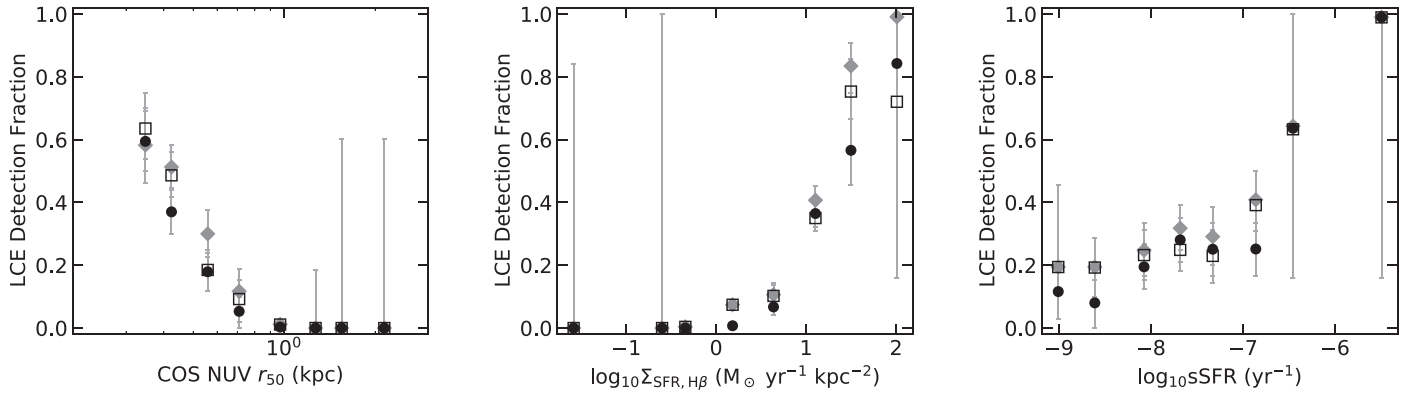

Figure 18. Same as Figure 2, but for r_{50}, Σ_{SFR}, and sSFR.

diagnostics to high redshift and for interpreting the distributions we observe.

One of the most contentious issues regarding reionization is the mass regime of galaxies that provide the ionizing photons. Some simulations predict that f_{esc}^{LyC} decreases with stellar mass (e.g., Kimm & Cen 2014) and UV luminosity (e.g., Trebitsch et al. 2017; Secunda et al. 2020), while others predict that f_{esc}^{LyC} increases with stellar mass and UV luminosity (e.g., Ma et al. 2020). The strongest LCEs in the combined sample of local LCEs are smaller, fainter galaxies with $M_\star \lesssim 10^9\ M_\odot$ and $M_{FUV} \gtrsim -19$. Reionization is likely driven by galaxies with similar properties.

The LzLCS samples the upper end of the simulated $M_\star - \Sigma_{SFR}$ distribution of LCEs in Naidu et al. (2020). We find that the combined sample of LCEs is largely consistent with their predictions, including the range in f_{esc}^{LyC}. However, our average f_{esc}^{LyC} toward higher stellar mass bins is about 0.1 dex lower than theirs even if considering only the strongest LCEs. Moreover, although we find qualitative agreement between the envelope in f_{esc}^{LyC} with respect to Σ_{SFR} and the $f_{esc}^{LyC} \propto \Sigma_{SFR}^{0.42}$ relation prescribed by Naidu et al. (2020), the $M_{1500} < -20$ LCEs in the LzLCS are not strong leakers at the same rate as their $M_{1500} > -19$ counterparts. While seemingly contrary to predictions by Naidu et al. (2020), the fact that brighter, higher-mass galaxies are less likely to be prodigious LCEs in our sample may be consistent with their simulations, as intermediate-mass galaxies at $z > 4$ tend to have emission-line properties similar to those of the $z \sim 0.3$ low-mass galaxies of this study. The $f_{esc}^{LyC} - \Sigma_{SFR}$ envelope also agrees with the sharp increase in f_{esc}^{LyC} predicted by Sharma et al. (2017), although we do not see the 20% f_{esc}^{LyC} values they suggest for $M_\star > 10^9\ M_\odot$. This might suggest that properties in addition to Σ_{SFR} (e.g., metallicity, dust) affect LyC escape.

O_{32} is a more empirical measurement than $M_\star$ or Σ_{SFR} and directly traces the ionization parameter. Together, these attributes have favored O_{32} as an f_{esc}^{LyC} diagnostic in the past. Unfortunately, properties like Σ_{SFR} and metallicity can also contribute to O_{32}, thus making interpretation of O_{32} unclear (see Nakajima & Ouchi 2014). As with the LzLCS, recent studies have found substantial scatter in the $f_{esc}^{LyC} - O_{32}$ diagnostic (e.g., Izotov et al. 2018b; Bassett et al. 2019), which Bassett et al. (2019) attribute to a combination of orientation and opening angle effects. With these physical and empirical caveats in mind, recent cosmological hydrodynamic simulations have predicted where high-redshift LCEs should appear in the $O_{32} - R_{32}$ diagnostic (e.g., Katz et al. 2020). We show the distribution of LzLCS (Izotov et al. 2016a, 2016b, 2018a, 2018b, 2021; Wang et al. 2019) and published LCEs (de Barros et al. 2016; Nakajima et al. 2020) and LAEs (Reddy et al. 2022) at $z \sim 2-3$ in Figure 26, along with $z \in [0.2, 0.4]$ star-forming galaxies taken from the Thomas et al. (2013) SDSS catalog for comparison. Simulations by Barrow et al. (2020) suggest that the entire distribution of LCEs shifts 0.5 dex lower in R_{23} at high redshift owing to decreases in metallicity while maintaining high O_{32} through high ionization parameter. On the other hand, simulations by Katz et al. (2020) suggest that LCEs at high redshift shift to a locus $\sim$1 dex higher in O_{32} than that of the SDSS galaxies, intersecting the low-metallicity "tail" where the combined low-redshift LCEs reside.

In contrast to these theoretical predictions, LCEs at moderate redshift ($z \sim 3$; Nakajima et al. 2020) still reside in this tail, despite having f_{esc} values in excess of 10%. Thus, even in earlier epochs, properties like age, ionization parameter, and metallicity may continue to outweigh the effects of LyC escape in setting O_{32}. Star-forming galaxies from the MOSDEF survey at $z \sim 2-3$ have O_{32} values more consistent with non-LCEs and typical SDSS star-forming galaxies. These galaxies are likely analogous to LBGs, suggesting that LBGs are only weakly leaking, if at all. Reddy et al. (2022) find that these galaxies have older burst ages (continuous star formation ages of $\sim$100 Myr), moderate ionization parameters ($\log U \sim -3$), and relatively higher metallicities ($\sim$30%–40% solar), which could readily account for the observed O_{32} values. These same properties may be associated with low levels of LyC escape. The LzLCS results suggest that O_{32} and f_{esc}^{LyC} may be indirectly related, as both O_{32} and f_{esc}^{LyC} may depend on the same physical properties, such as ionization parameter and metallicity. As such, these underlying properties will predominantly determine the observed O_{32} flux ratio at $z \sim 3$ and at $z \sim 6$.

5.3. Implications for High Redshift

One of the principal objectives of the LzLCS is to ascertain which diagnostics are best suited to identifying LCEs and inferring their f_{esc}^{LyC}. While $f_{esc}^{Ly\alpha}$, EW Lyα, v_{sep}, O_{32}, β_{1200}, NUV r_{50}, and Σ_{SFR} all exhibit strong significant correlations with f_{esc}^{LyC} at $z \sim 0.3$, comparisons with observations of these properties at higher redshifts are necessary to extend our results to the epoch of reionization.

Lyα offers one of the most promising indicators of LyC escape: both $f_{esc}^{Ly\alpha}$ and Lyα EW correlate well with f_{esc}^{LyC}, at least in part because Lyα is also sensitive to the line-of-sight

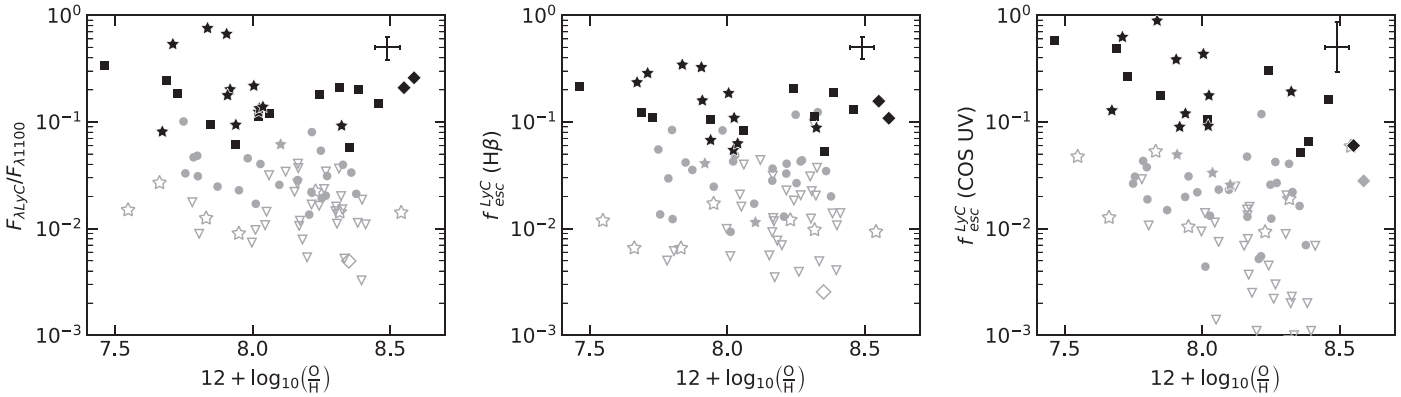

Figure 19. Same as Figure 1, but for gas-phase metallicity $12 + \log_{10}(O/H)$.

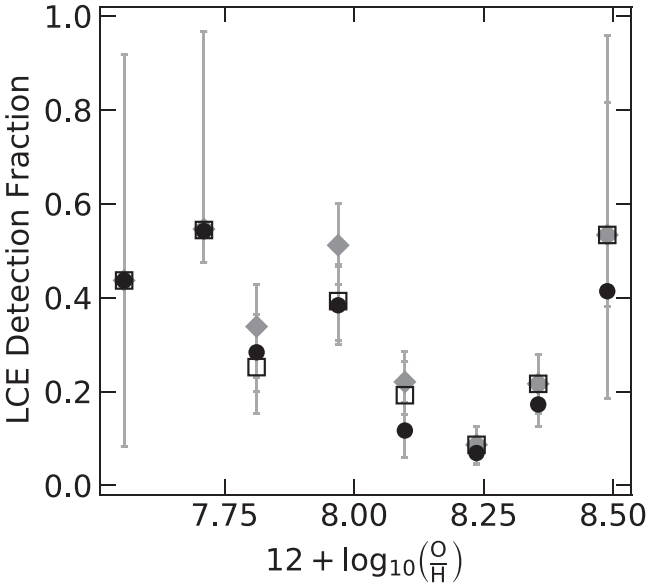

Figure 20. Same as Figure 2, but for $12 + \log_{10}(O/H)$.

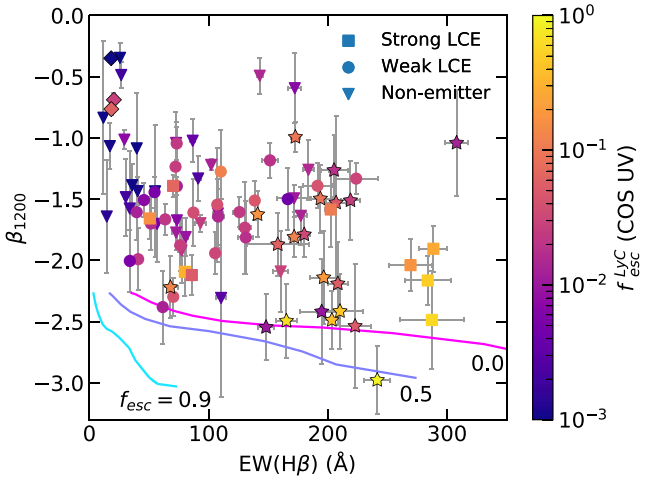

Figure 21. UV β_{1200} vs. Hβ EW for the LzLCS strong (squares) and weak (circles) LCEs and nonemitters (triangles) color-coded by f_{esc}^{LyC} derived from the UV spectrum. Solid lines are the Zackrisson et al. (2013) ∼30% solar-metallicity picket fence model predictions for $f_{esc}^{LyC} = 0.0$ (magenta), 0.5 (purple), and 0.9 (cyan). There appears to be no association of f_{esc}^{LyC} with a particular sequence in the UV β_{1200}–EW(Hβ) plane. While symbols are color-coded by the UV-fit f_{esc}^{LyC}, the observed trends here and in subsequent figures are similar if one of the other f_{esc}^{LyC} metrics is used.

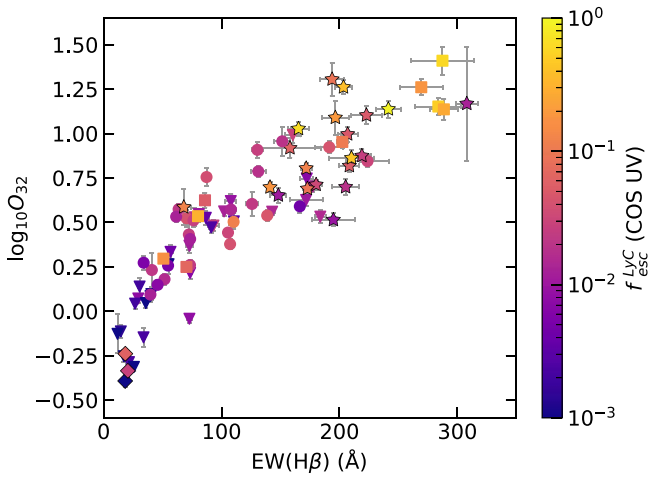

Figure 22. O_{32} vs. Hβ EW. Symbols are the same as in Figure 21. A strong correlation is evident, owing to the coupling of ionization parameter with starburst age.

neutral hydrogen column density. However, this sensitivity complicates the detection of Lyα because the neutral hydrogen fraction in the IGM increases dramatically with redshift (Tang et al. 2019; Thomas et al. 2021), accounting for the steep drop in LAEs observed at $z \gtrsim 6$ (e.g., Pentericci et al. 2011; Treu et al. 2013; Schenker et al. 2014). Although Lyα falls in the optical observing window at redshifts of $z \sim 6$, few Lyα emitters may be observable (an effect exacerbated by the shift of Lyα into the near-infrared at $z > 7$). But it does suggest that LCEs are frequently LAEs. The few LAEs detected at $z > 6$ may be leaking LyC. Indeed, the size of ionized bubbles necessary to produce observed double-peaked Lyα at $z \sim 6$ implies LyC escape (Meyer et al. 2021).

Star-forming galaxies observed at higher redshifts allow a more direct comparison with the LCEs from our sample. The $z \sim 2-3$ LBG-like star-forming galaxies from Reddy et al. (2022) have lower $f_{esc}^{Ly\alpha}$ and EW Lyα than the $z \sim 0.3$ LCEs, suggesting that LBGs are either extremely weak LCEs or nonemitters. The $z \sim 3$ individual LCEs from Nakajima et al. (2020) and $z \sim 2-3$ stacked spectra LCEs with $f_{esc}^{LyC} \geqslant 0.2$ from Steidel et al. (2018), Pahl et al. (2021), and Naidu et al. (2022) exhibit Lyα EWs of 30–110 Å and LyC escape fractions slightly larger than those of $z \sim 0.3$ LCEs at similar EWs. As shown in Figure 3, the Pahl et al. (2021) relation between f_{esc}^{LyC} and EW Lyα (based on the $z \sim 3$ stacks from

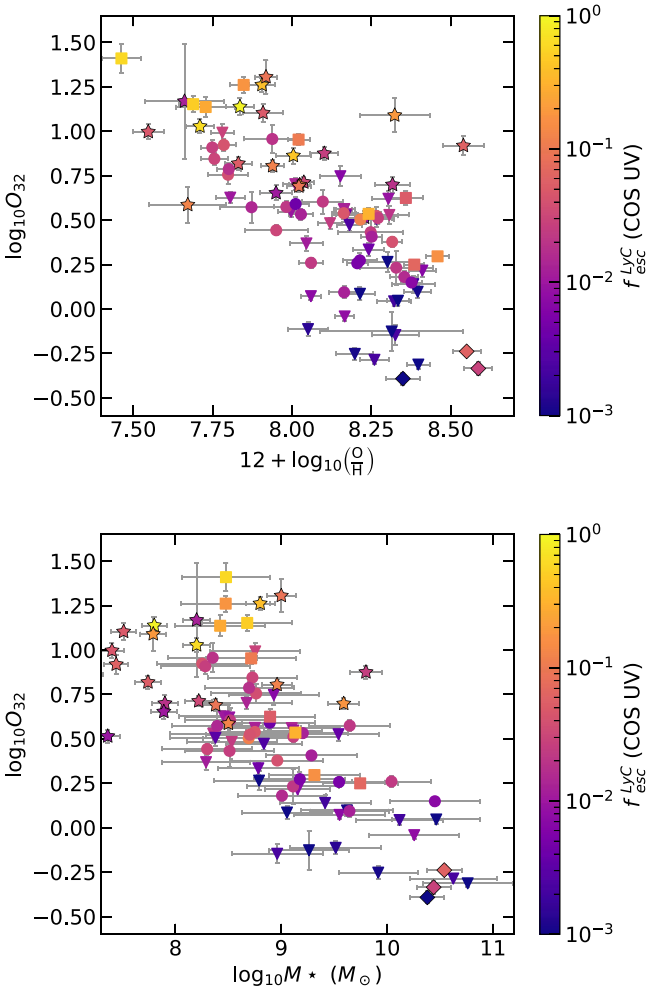

Figure 23. O_{32} compared to metallicity indicator $12 + \log_{10}(O/H)$ and SFH indicator $M_\star$. Symbols are the same as in Figure 21.

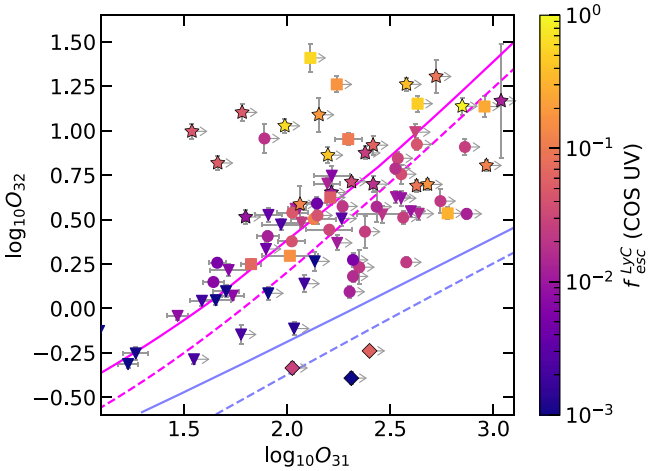

Figure 24. O_{32} vs. O_{31}. Symbols are the same as in Figure 21. Shown are the Stasińska et al. (2015) predictions for a 2 Myr starburst in a filled sphere (solid) and a spherical shell (dashed) nebula bounded by radiation (magenta) and density (purple). As a burst ages, O_{32} decreases at a fixed O_{31}.

Steidel et al. 2018) is qualitatively consistent with the f_{esc}^{LyC}–Lyα envelope in the LzLCS galaxies.

At higher redshifts, the Marchi et al. (2018) analysis of stacked spectra of $z = 3.5$–4.3 LAEs indicates that galaxies

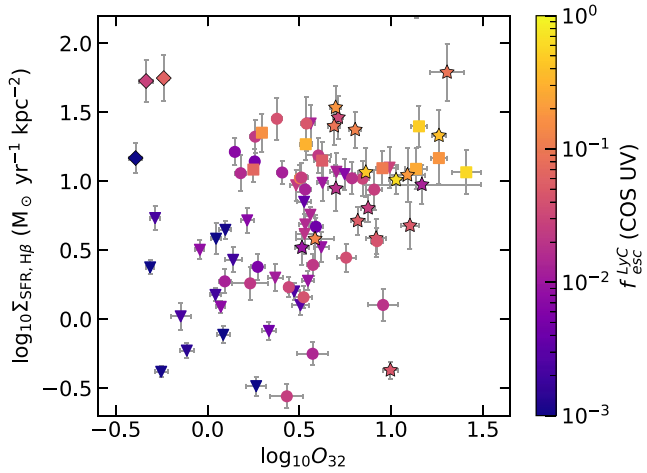

Figure 25. Σ_{SFR} vs. O_{32}. Symbols are the same as in Figure 21.

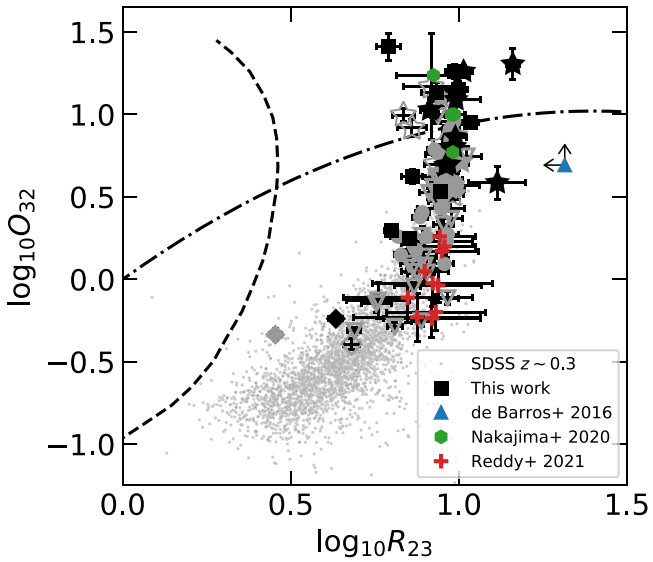

Figure 26. The O_{32} vs. R_{23} diagnostic for the combined sample. Symbols are the same as in Figures 1–19, with the addition of LCEs from Nakajima et al. (2020) with measured O_{32} and R_{23} (green hexagons), the $z = 3.2$ LCE from de Barros et al. (2016; blue triangle), and the $z = 1.85$–3.49 star-forming galaxies from the MOSDEF survey from Reddy et al. (2022; red plus signs). For reference, we show SDSS star-forming galaxies (gray circles) selected from the value-added catalog of Thomas et al. (2013) with requirements that $z \in [0.2, 0.4]$ and that strong emission lines have $F/\sigma > 3$. We show the locus of high-redshift LCEs predicted from cosmological simulations by Katz et al. (2020; dashed–dotted) and Barrow et al. (2020; dashed).

with Lyα EWs $\geqslant 50$ Å have relative f_{esc}^{LyC} significantly higher than 0.05, while those with Lyα EWs < 50 Å do not. The individual LyC detection in *Ion3* at $z = 4$ exhibits quadruply peaked Lyα with an EW of $\sim$40 Å and a relative escape fraction of 0.6 (Vanzella et al. 2018). These $z \sim 2$–4 results are consistent with the fact that 22/26 of the LzLCS strong LCEs have EW Ly$\alpha > 40$ Å. Thus, EW Lyα as an LCE identifier and f_{esc}^{LyC} diagnostic should be readily extensible to the epoch of reionization.

Studies by Steidel et al. (2018) and Pahl et al. (2021) at $z \sim 3$ suggest that fainter galaxies have higher f_{esc}^{LyC}. As shown in Section 3.5, we only find weak correlations with M_{1500}, although we do see a possible dependence of maximal f_{esc}^{LyC} on M_{1500}. That being said, our sample probes fainter magnitudes than studies at higher redshifts. Saldana-Lopez et al. (2022)

found that individual LCE detections at higher redshifts are consistent with LzLCS results for $F_{\lambda LyC}/F_{\lambda 1500}$ (see their Figure 16). LyC measurements using stacked spectra from Steidel et al. (2018) suggest that a possible envelope in $F_{\lambda LyC}/F_{\lambda 1500}$ persists out to $M_{1500} \sim -22$. Despite scatter, the increase in max $F_{\lambda LyC}/F_{\lambda 1500}$ with magnitude suggests that M_{1500} may still be a useful tool to estimate galaxy contributions to reionization. However, additional observations of UV-faint LCEs at $z \sim 3$ are necessary to confirm that the dependence of maximal $F_{\lambda LyC}/F_{\lambda 1100}$ on M_{1500} at $z \sim 3$ is similar to that observed in the combined LzLCS at $z \sim 0.3$.

Several indirect diagnostics driven by physical mechanism also show promise at high redshift. Star-forming galaxies at $z \sim 6-8$ have UV slopes and SFRs comparable to those of LCEs in this study (e.g., Bhatawdekar & Conselice 2021), which may suggest that the β_{1200} and Σ_{SFR} diagnostics at $z \sim 0.3$ can be used to identify LCEs and even infer f_{esc}^{LyC} at the epoch of reionization. Shibuya et al. (2015, 2019) find that star-forming galaxies become increasingly compact, approaching UV half-light radii of 0.5–0.7 kpc at $z \sim 6$. Such compactness is typical for the $z \sim 0.3$ LCEs in this study and LAEs in other studies (e.g., Kim et al. 2021). Moreover, this UV concentration corresponds to an average increase in Σ_{SFR} up to values $\gtrsim 10\ M_\odot\ \mathrm{yr}^{-1}\ \mathrm{kpc}^{-2}$ at $z \sim 6$ (Shibuya et al. 2015), which is comparable to the Σ_{SFR} of $z \sim 0.3$ LCEs. Such concentrated star formation at the epoch of reionization may be indicative of LyC escape. Star-forming galaxies at $z \sim 5-6$ could have higher-velocity outflows than galaxies of the same SFRs and stellar masses at $z \sim 0$ (Sugahara et al. 2019). Such extreme outflows might indicate augmented stellar feedback, in turn improving LyC escape indicators like Σ_{SFR}, $M_\star$, and UV β at $z \sim 6$ relative to $z \sim 0.3$.

The effect of gravity on f_{esc}^{LyC} diagnostics is not straightforward. In Section 3.7, we found no correlation of f_{esc}^{LyC} with $M_\star$. We did find a significant trend between f_{esc}^{LyC} and sSFR in Section 3.8, which may indicate that strong feedback better facilitates LyC escape in weaker gravitational potentials. At $z \sim 2.3$ (Sanders et al. 2016), $z \sim 3$ (Reddy et al. 2022), and $z = 7$ (Endsley et al. 2021), galaxies tend to have sSFR in the 1–10 Gyr^{-1} range, which corresponds to weaker LCEs and nonemitters at $z \sim 0.3$. Taking the Section 3.8 results at face value, these higher-redshift galaxies might not be prodigious LCEs. However, the analysis by Saxena et al. (2022) of individual LCEs at $z \sim 3$ suggests that galaxies with lower sSFR values of 1–10 Gyr^{-1} have f_{esc}^{LyC} in excess of 10% at higher redshift. No $z \sim 0.3$ LCEs with $f_{esc}^{LyC} > 10\%$ have sSFR $< 10\ \mathrm{Gyr}^{-1}$. This striking difference at $z \sim 3$ may point to an increase in burst-enabled LyC escape with redshift.

Other properties may readily persist at higher redshifts (e.g., Hβ EW, [O III] λ5007 EW, O_{32}, R_{23}; see Nakajima et al. 2020; Boyett et al. 2021; Endsley et al. 2021; Reddy et al. 2022; Saxena et al. 2022) but are difficult to observe at $z \gtrsim 6$ without space-based facilities like JWST. However, as we enter the JWST era, indirect indicators of f_{esc}^{LyC} will prove immensely useful via the trends presented in Section 3. Indeed, unlike observing the LyC, the reionization of the IGM is relatively insensitive to the anisotropic escape of LyC photons. The broad range of LCE properties may still complicate interpreting some diagnostics, as might the interdependent nature of parameters, since it is not clear how either will differ at $z \sim 6$.

LCEs at the epoch of reionization could be intrinsically unlike those in the LzLCS. Dust and the corresponding attenuation laws might alter the optical depth of the ISM at the epoch of reionization. Low metallicities in the early universe could suppress fragmentation during star formation, resulting in a top-heavy IMF with higher concentrations of O and B stars than at low redshift for the same Σ_{SFR}. Thus, a more physically complete understanding of the ISM and star formation at high redshift is paramount to successfully interpreting the signatures of LyC escape. Nevertheless, we find that young ages, concentrated star formation, and high ionization parameter are important for LyC escape.

6. Conclusion

Using the results for the 66 galaxies at $z \sim 0.3$ in the LzLCS, we have conducted the first thorough statistical test of indirect diagnostics of f_{esc}^{LyC} and LyC escape. We find that $f_{esc}^{Ly\alpha}$, EW Lyα, v_{sep}, O_{32}, EW Hβ, β_{1200}, $M_{1500,int}$, NUV r_{50}, Σ_{SFR}, and Σ_{sSFR} provide the best correlations with f_{esc}^{LyC}. However, many of these diagnostics exhibit an upper limit in the values of f_{esc}^{LyC} that varies with the property in question. We interpret these results as underlying trends that are obscured by a combination of line-of-sight effects and variations in other physical properties. Indirect diagnostics arising from stellar feedback mechanisms (e.g., stellar winds, SNe) tend to suffer from this effect more so than those based on optical depth. Such mechanism-based trends are still useful to infer f_{esc}^{LyC} while also providing insight into the nature of LyC escape. We note that the apparent success of each diagnostic may depend on the f_{esc}^{LyC} metric used, with templates fit to the COS spectra giving the strongest, most significant correlations of properties with f_{esc}^{LyC}. Since many of the trends show significant scatter for any given diagnostic parameter, we also perform a quantitative assessment of the fraction of galaxies that are LCEs.

Our statistical tests include the following diagnostics: fraction of Lyα photons ($f_{esc}^{Ly\alpha}$) that escape the host galaxy, EW(Lyα), the velocity separation (v_{sep}) between the Lyα profile peaks, the [O I] λ6300/Hβ flux ratio, the [O III] λ5007/[O I] λ6300 = O_{31} flux ratio, the [O III] λ5007/[O II] $\lambda\lambda$3726, 3729 = O_{32} flux ratio, EW(Hβ), M_{1500}, UV power-law slope β_{1200}, host galaxy stellar mass $M_\star$, half-light radius r_{50}, Σ_{SFR}, and sSFR = SFR/$M_\star$.

Of these diagnostics, $f_{esc}^{Ly\alpha}$, EW Lyα, v_{sep}, O_{32}, β_{1200}, NUV r_{50}, and Σ_{SFR} exhibit some of the strongest, most significant correlations with f_{esc}^{LyC}. Trends in f_{esc}^{LyC} with Lyα properties like $f_{esc}^{Ly\alpha}$, EW Lyα, and v_{sep} suggest that line-of-sight optical depth plays a key role in identifying LCEs and inferring f_{esc}^{LyC}. Other diagnostics, including O_{32}, r_{50}, Σ_{SFR}, and β_{1200}, also demonstrate strong, significant correlations with f_{esc}^{LyC}, indicating that concentrated star formation, young stellar populations, and high ionization play pivotal roles in LyC escape.

From these diagnostics, we have obtained deeper insight into the nature of LCEs and the conditions that may best facilitate LyC escape. LCEs tend to have compact ($r_{50} < 0.5$ kpc) regions of intense star formation ($\Sigma_{SFR} \gtrsim 10\ M_\odot\ \mathrm{yr}^{-1}\ \mathrm{kpc}^{-2}$), indicating that stellar feedback may be crucial for LyC escape.

The distribution of f_{esc}^{LyC} over other properties like ionization parameter (measured by O_{32}), burst age (measured by Hβ EW), stellar mass, and metallicity suggests a broad range in LCE galaxy properties that persists across many diagnostics. This diversity suggests that different physical conditions can lead to LyC escape or that a time delay between star formation and LyC escape can decouple f_{esc}^{LyC} from certain galaxy properties.

With that being said, galaxies with high O_{32}, high Hβ EW, and low β are more likely to be strong LCEs ($f_{esc}^{LyC} \gtrsim 0.05$), suggesting that galaxies like the GPs are the most substantial LyC leakers.

To better understand how certain properties can affect one another and the inferred f_{esc}^{LyC}, we juxtapose f_{esc}^{LyC} diagnostics. Zackrisson et al. (2013) proposed a comparison of β_{1200} with EW(Hβ). We find that, while not following the predictions from Zackrisson et al. (2013), LCEs with higher f_{esc}^{LyC} tend to have higher EW(Hβ) (>100 Å) and steeper UV continua (< −2). Moreover, LCEs distinguish themselves as having either higher EW(Hβ) and steeper UV continua or lower EW(Hβ) (<100 Å) and more shallow UV continua (>−2).

We also compare O_{32} and EW(Hβ), finding that the two are strongly correlated. Through comparisons with mass and metallicity, we find that higher O_{32} (>5), higher f_{esc}^{LyC} LCEs have low masses and low metallicities, while the lower O_{32} (<5), lower f_{esc}^{LyC} LCEs have higher masses and higher metallicities. These results point to a distinct difference in LyC escape mechanism, as discussed above. The oxygen ionization structure indicated by O_{32} and O_{31} (e.g., Stasińska et al. 2015) demonstrates that LCEs cannot be readily described by a simple density-bounded, isotropic escape scenario. Even so, all LCEs display concentrated star formation, indicating that locally intense star formation is necessary for LyC escape regardless of mechanism.

For further insight into LCEs, we compare our results with cosmological and galaxy evolution simulation predictions. Consistent with some simulations (e.g., Trebitsch et al. 2017; Secunda et al. 2020), we demonstrate that compact, UV-faint, low-mass galaxies are far more likely to be significant LyC leakers than other galaxies. While we do find that concentrated star formation is a significant indicator of LyC escape, simulations that predict this relationship suggest that LCEs ought to have higher stellar masses than we find in our sample (e.g., Sharma et al. 2017; Nakajima et al. 2020).

While we demonstrate that Lyα is the best f_{esc}^{LyC} indicator at low redshift and that our LCEs are comparable to LyC-leaking LAEs at $z \sim 2-3$, the increasing IGM opacity at $z \gtrsim 4$ renders Lyα, at best, difficult to detect from galaxies at the epoch of reionization. From a holistic interpretation of other indirect diagnostics, a galaxy with high EW Lyα, high $f_{esc}^{Ly\alpha}$, high O_{32}, high EW(Hβ), low β_{1200}, low NUV r_{50}, and high Σ_{SFR} is likely an LCE. Thus, observing rest-frame properties like O_{32}, EW(Hβ), and Σ_{SFR} with JWST is critical to identifying and understanding the galaxies responsible for cosmic reionization.

Support for this work was provided by NASA through grant No. HST-GO-15626 from the Space Telescope Science Institute. Additional work was based on observations made with the NASA/ESA Hubble Space Telescope, obtained from the data archive at the Space Telescope Science Institute from HST proposals 13744, 14635, 15341, and 15639. STScI is operated by the Association of Universities for Research in Astronomy, Inc. under NASA contract NAS 5-26555.

Funding for the Sloan Digital Sky Survey IV has been provided by the Alfred P. Sloan Foundation, the U.S. Department of Energy Office of Science, and the Participating Institutions. SDSS-IV acknowledges support and resources from the Center for High Performance Computing at the University of Utah. The SDSS website is www.sdss.org. SDSS-IV is managed by the Astrophysical Research Consortium for the Participating Institutions of the SDSS Collaboration.

R.A. acknowledges support from ANID Fondecyt Regular 1202007.

Software: ASTROPY (Astropy Collaboration et al. 2013, 2018), MATPLOTLIB (Hunter 2007), NUMPY (van der Walt et al. 2011), SCIPY (Virtanen et al. 2020).

ORCID iDs

Sophia R. Flury https://orcid.org/0000-0002-0159-2613
Anne E. Jaskot https://orcid.org/0000-0002-6790-5125
Harry C. Ferguson https://orcid.org/0000-0001-7113-2738
Gábor Worseck https://orcid.org/0000-0003-0960-3580
Kirill Makan https://orcid.org/0000-0003-3157-1191
John Chisholm https://orcid.org/0000-0002-0302-2577
Daniel Schaerer https://orcid.org/0000-0001-7144-7182
Stephan R. McCandliss https://orcid.org/0000-0003-0503-4667
Xinfeng Xu https://orcid.org/0000-0002-9217-7051
Bingjie Wang https://orcid.org/0000-0001-9269-5046
M. S. Oey https://orcid.org/0000-0002-5808-1320
N. M. Ford https://orcid.org/0000-0001-8921-3624
Timothy Heckman https://orcid.org/0000-0001-6670-6370
Zhiyuan Ji https://orcid.org/0000-0001-7673-2257
Mauro Giavalisco https://orcid.org/0000-0002-7831-8751
Ricardo Amorín https://orcid.org/0000-0001-5758-1000
Sanchayeeta Borthakur https://orcid.org/0000-0002-2724-8298
Cody Carr https://orcid.org/0000-0003-4166-2855
Marco Castellano https://orcid.org/0000-0001-9875-8263
Stephane De Barros https://orcid.org/0000-0002-5877-8793
Mark Dickinson https://orcid.org/0000-0001-5414-5131
Steven L. Finkelstein https://orcid.org/0000-0001-8519-1130
Brian Fleming https://orcid.org/0000-0002-2129-0292
Fabio Fontanot https://orcid.org/0000-0003-4744-0188
Andrea Grazian https://orcid.org/0000-0002-5688-0663
Matthew Hayes https://orcid.org/0000-0001-8587-218X
Alaina Henry https://orcid.org/0000-0002-6586-4446
Genoveva Micheva https://orcid.org/0000-0003-4376-2841
Goran Ostlin https://orcid.org/0000-0002-3005-1349
Casey Papovich https://orcid.org/0000-0001-7503-8482
Laura Pentericci https://orcid.org/0000-0001-8940-6768
Michael Rutkowski https://orcid.org/0000-0001-7016-5220
Paola Santini https://orcid.org/0000-0002-9334-8705
Claudia Scarlata https://orcid.org/0000-0002-9136-8876
Harry Teplitz https://orcid.org/0000-0002-7064-5424
Maxime Trebitsch https://orcid.org/0000-0002-6849-5375
Eros Vanzella https://orcid.org/0000-0002-5057-135X

References

Akritas, M. G., & Siebert, J. 1996, MNRAS, 278, 919
Alavi, A., Colbert, J., Teplitz, H. I., et al. 2020, ApJ, 904, 59
Alexandroff, R. M., Heckman, T. M., Borthakur, S., Overzier, R., & Leitherer, C. 2015, ApJ, 810, 104
Astropy Collaboration, Price-Whelan, A. M., & SipHocz, B. M. 2018, AJ, 156, 123
Astropy Collaboration, Robitaille, T. P., Tollerud, E. J., et al. 2013, A&A, 558, A33
Bagley, M. B., Scarlata, C., Henry, A., et al. 2017, ApJ, 837, 11
Barrow, K. S. S., Robertson, B. E., Ellis, R. S., et al. 2020, ApJ, 902, 39
Bassett, R., Ryan-Weber, E. V., Cooke, J., et al. 2019, MNRAS, 483, 5223
Becker, R. H., Fan, X., White, R. L., et al. 2001, AJ, 122, 2850

Behrens, C., Dijkstra, M., & Niemeyer, J. C. 2014, A&A, 563, A77
Bergvall, N., Leitet, E., Zackrisson, E., & Marquart, T. 2013, A&A, 554, A38
Bhatawdekar, R., & Conselice, C. J. 2021, ApJ, 909, 144
Binggeli, C., Zackrisson, E., Pelckmans, K., et al. 2018, MNRAS, 479, 368
Boyett, K. N. K., Stark, D. P., Bunker, A. J., Tang, M., & Maseda, M. V. 2021, arXiv:2110.15858
Byrohl, C., & Gronke, M. 2020, A&A, 642, 16
Cardelli, J. A., Clayton, G. C., & Mathis, J. S. 1989, ApJ, 345, 245
Castellano, M., Pentericci, L., Fontana, A., et al. 2017, ApJ, 839, 73
Cen, R., & Kimm, T. 2015, ApJL, 801, L25
Chisholm, J., Orlitová, I., Schaerer, D., et al. 2017, A&A, 605, A67
Chisholm, J., Rigby, J. R., Bayliss, M., et al. 2019, ApJ, 882, 182
Clarke, C., & Oey, M. S. 2002, MNRAS, 337, 1299
de Barros, S., Vanzella, E., Amorín, R., et al. 2016, A&A, 585, A51
Dijkstra, M., Gronke, M., & Venkatesan, A. 2016, ApJ, 828, 71
Endsley, R., Stark, D. P., Charlot, S., et al. 2021, MNRAS, 500, 5229
Finkelstein, S. L., Papovich, C., Ryan, R. E., et al. 2012, ApJ, 758, 93
Fletcher, T. J., Tang, M., Robertson, B. E., et al. 2019, ApJ, 878, 87
Flury, S. R., Jaskot, A. E., Ferguson, H. C., et al. 2022, ApJS, 260, 1
Gazagnes, S., Chisholm, J., Schaerer, D., Verhamme, A., & Izotov, Y. 2020, A&A, 639, A85
Gehrels, N. 1986, ApJ, 303, 336
Guo, Y., Rafelski, M., Faber, S. M., et al. 2016, ApJ, 833, 37
Hayes, M. J., Runnholm, A., Gronke, M., & Scarlata, C. 2021, ApJ, 908, 36
Heckman, T. M., Borthakur, S., Overzier, R., et al. 2011, ApJ, 730, 5
Heckman, T. M., Sembach, K. R., Meurer, G. R., et al. 2001, ApJ, 558, 56
Henry, A., Scarlata, C., Martin, C. L., & Erb, D. 2015, ApJ, 809, 19
Hunter, J. D. 2007, CSE, 9, 90
Izotov, Y. I., Orlitová, I., Schaerer, D., et al. 2016a, Natur, 529, 178
Izotov, Y. I., Schaerer, D., Thuan, T. X., et al. 2016b, MNRAS, 461, 3683
Izotov, Y. I., Schaerer, D., Worseck, G., et al. 2018a, MNRAS, 474, 4514
Izotov, Y. I., Schaerer, D., Worseck, G., et al. 2020, MNRAS, 491, 468
Izotov, Y. I., Thuan, T. X., & Guseva, N. G. 2017, MNRAS, 471, 548
Izotov, Y. I., Worseck, G., Schaerer, D., et al. 2018b, MNRAS, 478, 4851
Izotov, Y. I., Worseck, G., Schaerer, D., et al. 2021, MNRAS, 503, 1734
Jaskot, A. E., Dowd, T., Oey, M. S., Scarlata, C., & McKinney, J. 2019, ApJ, 885, 96
Jaskot, A. E., & Oey, M. S. 2013, ApJ, 766, 91
Jaskot, A. E., Oey, M. S., Scarlata, C., & Dowd, T. 2017, ApJL, 851, L9
Ji, Z., Giavalisco, M., Vanzella, E., et al. 2020, ApJ, 888, 109
Johnson, B. D., Leja, J. L., Conroy, C., & Speagle, J. S. 2019, Prospector: Stellar population inference from spectra and SEDs, Astrophysics Source Code Library, ascl:1905.025
Kakiichi, K., & Gronke, M. 2021, ApJ, 908, 30
Katz, H., Ďurovčíková, D., Kimm, T., et al. 2020, MNRAS, 498, 164
Kennicutt, R. C., & Evans, N. J. 2012, ARA&A, 50, 531
Kim, K. J., Malhotra, S., Rhoads, J. E., & Yang, H. 2021, ApJ, 914, 2
Kimm, T., & Cen, R. 2014, ApJ, 788, 121
Kobulnicky, H. A., & Kewley, L. J. 2004, ApJ, 617, 240
Laursen, P., Sommer-Larsen, J., & Razoumov, A. O. 2011, ApJ, 728, 52
Leitherer, C., Ortiz Otálvaro, P. A., Bresolin, F., et al. 2010, ApJS, 189, 309
Leja, J., Johnson, B. D., Conroy, C., van Dokkum, P. G., & Byler, N. 2017, ApJ, 837, 170
Ma, X., Quataert, E., Wetzel, A., et al. 2020, MNRAS, 498, 2001
Makan, K., Worseck, G., Davies, F. B., et al. 2021, ApJ, 912, 38
Marchi, F., Pentericci, L., Guaita, L., et al. 2018, A&A, 614, A11
Meyer, R. A., Laporte, N., Ellis, R. S., Verhamme, A., & Garel, T. 2021, MNRAS, 500, 558
Micheva, G., Oey, M. S., Jaskot, A. E., & James, B. L. 2017, ApJ, 845, 165
Naidu, R. P., Matthee, J., Oesch, P. A., et al. 2022, MNRAS, 510, 4582
Naidu, R. P., Tacchella, S., Mason, C. A., et al. 2020, ApJ, 892, 109
Nakajima, K., Ellis, R. S., Robertson, B. E., Tang, M., & Stark, D. P. 2020, ApJ, 889, 161
Nakajima, K., & Ouchi, M. 2014, MNRAS, 442, 900
Osterbrock, D., & Ferland, G. 2006, Astrophysics of Gaseous Nebulae and Active Galactic Nuclei (Mill Valley, CA: Univ. Science Books)
Paardekooper, J.-P., Khochfar, S., & Dalla Vecchia, C. 2015, MNRAS, 451, 2544
Pahl, A. J., Shapley, A., Faisst, A. L., et al. 2020, MNRAS, 493, 3194
Pahl, A. J., Shapley, A., Steidel, C. C., Chen, Y., & Reddy, N. A. 2021, MNRAS, 505, 2447
Paoletti, D., Hazra, D. K., Finelli, F., & Smoot, G. F. 2020, JCAP, 2020, 005
Pentericci, L., Fontana, A., Vanzella, E., et al. 2011, ApJ, 743, 132
Pilyugin, L. S., Thuan, T. X., & Vílchez, J. M. 2006, MNRAS, 367, 1139
Plat, A., Charlot, S., Bruzual, G., et al. 2019, MNRAS, 490, 978
Ramambason, L., Schaerer, D., Stasińska, G., et al. 2020, A&A, 644, A21
Razoumov, A. O., & Sommer-Larsen, J. 2010, ApJ, 710, 1239
Reddy, N. A., Steidel, C. C., Pettini, M., & Bogosavljević, M. 2016, ApJ, 828, 107
Reddy, N. A., Topping, M. W., Shapley, A. E., et al. 2022, ApJ, 926, 31
Rivera-Thorsen, T. E., Dahle, H., Chisholm, J., et al. 2019, Sci, 366, 738
Saldana-Lopez, A., Schaerer, D., Chisholm, J., et al. 2022, arXiv:2201.11800
Sanders, R. L., Shapley, A. E., Jones, T., et al. 2021, ApJ, 914, 19
Sanders, R. L., Shapley, A. E., Kriek, M., et al. 2016, ApJ, 816, 23
Sanders, R. L., Shapley, A. E., Reddy, N. A., et al. 2020, MNRAS, 491, 1427
Sawant, A. N., Pellegrini, E. W., Oey, M. S., López-Hernández, J., & Micheva, G. 2021, ApJ, 923, 78
Saxena, A., Pentericci, L., Ellis, R. S., et al. 2022, MNRAS, 511, 120
Schenker, M. A., Ellis, R. S., Konidaris, N. P., & Stark, D. P. 2014, ApJ, 795, 20
Secunda, A., Cen, R., Kimm, T., Gotberg, Y., & de Mink, S. E. 2020, ApJ, 901, 72
Sharma, M., Theuns, T., Frenk, C., et al. 2016, MNRAS, 458, L94
Sharma, M., Theuns, T., Frenk, C., et al. 2017, MNRAS, 468, 2176
Shibuya, T., Ouchi, M., & Harikane, Y. 2015, ApJS, 219, 15
Shibuya, T., Ouchi, M., Harikane, Y., & Nakajima, K. 2019, ApJ, 871, 164
Stasińska, G., Izotov, Y., Morisset, C., & Guseva, N. 2015, A&A, 576, A83
Steidel, C. C., Bogosavljević, M., Shapley, A. E., et al. 2018, ApJ, 869, 123
Storey, P. J., & Hummer, D. G. 1995, MNRAS, 272, 41
Strom, A. L., Steidel, C. C., Rudie, G. C., Trainor, R. F., & Pettini, M. 2018, ApJ, 868, 117
Sugahara, Y., Ouchi, M., Harikane, Y., et al. 2019, ApJ, 886, 29
Tang, M., Stark, D. P., Chevallard, J., & Charlot, S. 2019, MNRAS, 489, 2572
Thomas, D., Steele, O., Maraston, C., et al. 2013, MNRAS, 431, 1383
Thomas, R., Pentericci, L., Le Fèvre, O., et al. 2021, A&A, 650, A63
Trebitsch, M., Blaizot, J., Rosdahl, J., Devriendt, J., & Slyz, A. 2017, MNRAS, 470, 224
Tremonti, C. A., Heckman, T. M., Kauffmann, G., et al. 2004, ApJ, 613, 898
Treu, T., Schmidt, K. B., Trenti, M., Bradley, L. D., & Stiavelli, M. 2013, ApJL, 775, L29
van der Walt, S., Colbert, S. C., & Varoquaux, G. 2011, CSE, 13, 22
Vanzella, E., Caminha, G. B., Calura, F., et al. 2020, MNRAS, 491, 1093
Vanzella, E., Giavalisco, M., Dickinson, M., et al. 2009, ApJ, 695, 1163
Vanzella, E., Guo, Y., Giavalisco, M., et al. 2012, ApJ, 751, 70
Vanzella, E., Nonino, M., Cupani, G., et al. 2018, MNRAS, 476, L15
Verhamme, A., Orlitová, I., Schaerer, D., & Hayes, M. 2015, A&A, 578, A7
Verhamme, A., Orlitová, I., Schaerer, D., et al. 2017, A&A, 597, A13
Virtanen, P., Gommers, R., & Oliphant, T. E. 2020, NatMe, 17, 261
Wang, B., Heckman, T. M., Leitherer, C., et al. 2019, ApJ, 885, 57
Weisz, D. R., Johnson, B. D., Johnson, L. C., et al. 2012, ApJ, 744, 44
Wise, J. H., Demchenko, V. G., Halicek, M. T., et al. 2014, MNRAS, 442, 2560
Worseck, G., Prochaska, J. X., Hennawi, J. F., & McQuinn, M. 2016, ApJ, 825, 144
Worseck, G., Prochaska, J. X., O'Meara, J. M., et al. 2014, MNRAS, 445, 1745
Wyithe, J. S. B., & Loeb, A. 2013, MNRAS, 428, 2741
Yajima, H., Sugimura, K., & Hasegawa, K. 2018, MNRAS, 477, 5406
Yang, H., Malhotra, S., Gronke, M., et al. 2017a, ApJ, 844, 171
Yang, H., Malhotra, S., Rhoads, J. E., et al. 2017b, ApJ, 838, 4
Yang, J., Wang, F., Fan, X., et al. 2020, ApJ, 904, 26
Zackrisson, E., Binggeli, C., Finlator, K., et al. 2017, ApJ, 836, 78
Zackrisson, E., Inoue, A. K., & Jensen, H. 2013, ApJ, 777, 39
Zastrow, J., Oey, M. S., Veilleux, S., & McDonald, M. 2013, ApJ, 779, 76